SEMIEMPIRICAL MODIFIED EMBEDDED ATOM POTENTIALS FOR SILICON, SILVER AND GOLD SYSTEMS

MICHAEL COATES

Semiempirical Modified Embedded Atom Potentials for Silicon, Silver and Gold Systems

by

© Michael Coates

A thesis submitted to the

School of Graduate Studies

in partial fulfilment of the

requirements of the degree of

Master of Science

Department of Physics and Physical Oceanography

Memorial University of Newfoundland

August 2009

St. John's Newfoundland

Abstract

In this work, semiempirical interatomic potentials for silicon, gold, silver and their alloys have been developed, based on the modified embedded atom method (MEAM) formalism. These potentials describe the elastic, thermal, structural, point defect, and binary cluster properties as well as any other empirical potential, and exhibit good agreement with experimental data where available. Specifically, silicon potentials have been compared to the best available first and second nearest neighbour MEAM parameterizations, as well as the Stillinger-Weber, Tersoff, EDIP and HOEP potentials; silver and gold have been compared to first and second nearest neighbour MEAM. In the absence of experimental data, high level density functional theory (DFT) calculations have been used instead. Applications of these potentials for the specific case of microcantilever sensor fabrication and characterization have been outlined, including interfacial stress and surface analyses.

Acknowledgments

First and foremost, I would like to thank my supervisor, Dr. Luc Beaulieu, for the opportunity to continue my studies as a Masters student. Throughout my brief career, Dr. Beaulieu has provided endless support, insight and guidance. His unwavering encouragement has helped me through many difficult times, when the work seemed overwhelming and without end. His faith in my abilities, when I had none, has helped me to evolve as both a student and a teacher. In short, I owe my entire career to Dr. Beaulieu – it is my hope that my time at Memorial has been as rewarding for him as it has for me.

I would also like to thank my group members, past and present, for their support. During my time at Memorial, the group were always available to discuss problems, to lend a hand, to talk. I wish you all success in your studies, and hope that someday soon we might work together again.

I would like to thank the Department, especially Dr. Saika-Voivod, Dr. Kris Poduska and Dr. Anand Yethiraj for the thesis-related discussions (thermodynamics...) and teaching opportunities. Memorial offered me, a lowly Masters student, many opportunities to teach independently – these professors mentored me through the rough patches, and allowed me to mature as an instructor. I have a long way to go, but any steps I've made so far are thanks to you.

My family has also been crucial in my success – they have been extremely supportive of my choices (even the ones that haven't made sense) and have always been there in times of need. I could not have done this without you.

Finally, I would like to thank the granting agencies, specifically NSERC and ACENet, for funding my research.

Table of Contents

List of Tables

List of Figures

List of Symbols and Abbreviations

$\|lm>$	Spherical Harmonics
α_i	Adjustable Parameter in Rose Energy
α_l	Linear Coefficient of Thermal Expansion
β	Adjustable Decay Constants for Partial Electron Densities
ε	Strain Parameter
ε_i	Kohn-Sham Eigenvalue
ε_{XC}	XC Energy per Electron
ε_{XC}^{hom}	XC Energy per Electron in a Homogeneous Electron Gas
γ, γ'	Shear Elastic Constants
γ_G	Grüneisen Coefficient
ν	Poisson's Ratio
Ω	Unit Cell Volume
ρ	Density (Volumetric)
φ	Electrostatic Pair Potential
ψ_i	Wavefunction of Electronic State i
θ	Angle Between Atoms i, j, k
1NN	First Nearest Neighbour
2NN	Second Nearest Neighbour
A	Adjustable Parameter in Embedding Function

Ag	Silver
att	Adjustable Attractive Parameter for Rose Energy
Au	Gold
B	Bulk Modulus
B_0'	Bulk Modulus Pressure Derivative
BCC	Body Centered Cubic
C	Adjustable Parameters in Screening Function
c, a	Lattice Parameters
C_{11}, C_{12}, C_{11}	Elastic Constants
c_i	Bloch Coefficients
C_{ij}	Elastic Constant Tensor
C_V	Specific Heat Capacity
d	Plane Spacing
DFT	Density Functional Theory
Dia	Diamond Cubic
E	Energy
EAM	Embedded Atom Method
E_c	Correlation Energy
EDIP	Environment Dependent Interatomic Potential
E_{ion}	Coulomb Energy Associated with Ion Interactions
erfc	Complimentary Error Function
E_x	Exchange Energy
E_{xc}	Exchange-Correlation Functional

F	Embedding Function
FCC	Face Centered Cubic
$\mathcal{F}$	Embedding Functional
$\mathbf{G}$	Reciprocal Lattice Vectors
G	Shear Modulus
GGA	Generalized Gradient Approximation
$\hbar$	Normalised Planck Constant
HCP	Hexagonal Close Packed
HOEP	Highly Optimized Empirical Potential
k	Wavevector
K	Diatomic Force Constant
k_B	Boltzmann Constant
l	Real Space Lattice Vectors
LAMMPS	Large-scale Atomic Molecular Massively Parallel Simulator
LDA	Local Density Approximation
MAE	Mean Absolute Error
MEAM	Modified Embedded Atom Method
n	Electron Density
N	Number of Atoms
PBE	Perdew, Burke and Ernzerhof XC Functional
Q	Activation Energy of Vacancy Diffusion
$\mathbf{R}$	Nuclear Coordinates
rep	Adjustable Repulsive Parameter for Rose Energy

RRKJ	Rappe, Rabe, Kaxiras and Joannopoulos Pseudopotential
S	Sulfur
S	Screening Function
S'	Structure Factor
SC	Simple Cubic
Si	Silicon
S_{ij}	Inverse Elastic Constant Tensor
SW	Stillinger-Weber Pair Potential
t	Adjustable Weighting Functions for Partial Electron Densities
T_D	Debye Temperature
Ters	Tersoff Pair Potential
V	Volume
V_H	Hartree Potential of Electrons
V_{ion}	Static Electron-Ion Potential
V_l	Pseudopotential for Angular Momentum l
v_l	Longitudinal Sound Velocity
v_m	Mean Sound Velocity
v_t	Transverse Sound Velocity
V_{XC}	Exchange-Correlation Potential
x, y, z	Cartesian Coordinates
XC	Exchange-Correlation
Y	Young's Modulus
Z_i	Valence of Atom i

1. INTRODUCTION

Microcantilever sensors consist of a cantilever with dimensions 200-400 μm long, 30-50 μm wide and 1 μm thick, coated on one side with a receptive layer chemically engineered to bond only to a specific target molecule. These sensors have been successfully used as chemical sensors to detect liquid or gas-phase molecules [1 – 4], as biosensors to observe specific enzymes, antibodies, proteins and DNA chains [5 – 10], to determine stress associated with surface adsorption [11 – 13], to examine magnetic susceptibilities [14], and to measure pH [15]. In fact, microcantilever sensors are amongst the only sensors with the ability to detect quantities in the nanogram (10^{-9}), pictolitre (10^{-12}), femtojoule (10^{-15}) and attomolar(10^{-18}) range with a response time on the order of milliseconds (10^{-3}) [3].

To develop a microcantilever sensor, an intermediate tie layer is required between the silicon substrate and the organic receptor layer, as shown in Figure 1.1. Gold is often chosen for this purpose as, of all the metallic elements, it is the most chemically stable [16]. It is well known that organic molecules terminated with a sulfur end-group self-assemble onto gold surfaces and form strong, structurally stable molecular films [17]. However, it has been shown that the morphology of the underlying gold film plays an important role in both the sensitivity of the sensor and the reproducibility of the results [18]. Further, the surface stress arising due to mismatches in the thermal expansion coefficients between the film and substrate, nonuniform plastic deformations, lattice mismatches, substitutional or interstitial impurities and growth processes is directly related to the surface morphology of the

film [19]. In the case of microcantilevers, the deposition of a thin film(s) creates a surface stress which may cause the cantilever to either bend upwards or downwards [19 – 21].

Figure 1.1: Microcantilever schematic. A Silicon microcantilever (grey) is first coated with a metallic tie layer (yellow) to which an organic receptive layer (blue) is adsorbed. Not to scale.

Much work has been done in characterizing the observed surface stress as a function of deposition parameters (deposition rate, temperature, annealing time, etc.). Many groups have modeled surface stress for single, and multiple, films of varying thicknesses in an attempt to estimate the necessary film parameters [22 – 31]. Nonetheless, at this time no group has located a set of parameters which result in a cantilever without residual bending. Instead, researchers have focused on reducing residual stress post-fabrication by way of ion implantation and/or impurity doping paired with annealing [32 – 35].

The goal of this work is to develop a series of potentials which very accurately describe metallic thin films on a silicon substrate. These potentials will then be used, amongst other things, to predict the composition of the tie layer which yields no net interfacial stress and an atomically flat surface layer. For this purpose, the Modified Embedded Atom Method (MEAM) is chosen. The MEAM, discussed in depth in

Chapter 3, has the innate ability to treat covalent systems, such as silicon [36, 37] and metallic systems, such as silver and gold [38, 39] equally well. In addition, being a semi-empirical potential, it offers this accuracy at a lower computational cost than present *ab initio* techniques.

The silicon–gold system is quite complex. Distinguishing it from other noble metal-silicon pairs, such as silicon–silver and silicon–copper, is an unusually high reaction rate between these two species, which results in rapid diffusion across the interface, even at room temperature. The result of this extensive migration is an intermixing of silicon and gold atoms, and the formation of a silicide-like alloy at the interface. Despite extensive research, crucial features of this system remain unresolved. For instance, the critical thickness necessary for the onset of intermixing, the structure of the interface, the penetration depth of the gold/silicon atoms into the bulk and the surface composition and structure of thin monolayers are yet unknown. For an extensive review of the current research of the silicon–gold system, the reader is referred to [10]; these results are summarized schematically in Figure 1.2.

To avoid the complexities of the silicon–gold interface, it is also prudent to study the silicon–silver–gold system. It has been established that the silicon–silver system does not exhibit the high reaction rate of the silicon–gold system, and as such should provide a more stable and predictable base for the topmost gold layer. In addition, the physical features of silver and gold are quite comparable. For instance, the lattice constant, bulk modulus and coefficient of linear thermal expansion are 4.09 Å, 108.7 GPa, and 19.1×10^{-6} K^{-1} for silver and 4.08 Å, 108.3 GPa and 14.1×10^{-6} K^{-1} for gold, respectively. Given the similarities between these two species, interfacial stresses due to, for example, lattice, elastic and thermal expansion mismatches

should be minimal. Hence, it is hypothesized that the complexities of the silicon–gold system may be altogether avoided at a slight cost to interfacial stress.

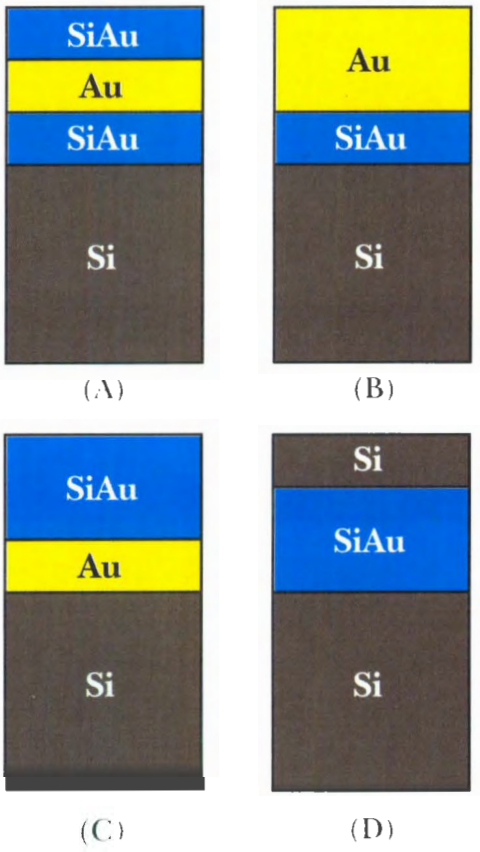

Figure 1.2: Schematic representation of the experimentally proposed SiAu interface structures for thin ($\leq$ 10 ML) gold films. Measurements are taken using: (A) AES-LEED and TEM [41, 42]; (B) MeV ion scattering and PAES [43 – 45]; (C) PYS and SRPS [46 – 48]; (D)XPS [49].

To accurately fit the MEAM potential, one requires an excess of experimental data. While an abundance of data is available for the individual elements (Si, Ag and Au), the same cannot be said for the alloys SiAg, SiAu and SiAgAu. None of these compounds form a thermodynamically stable structure. As such, a high level of theory must be used to predict values to which to fit the MEAM potential. Density

functional theory is chosen for this purpose; it will now be discussed in the subsequent chapter.

In the chapters which remain, the Modified Embedded Atom Method theory will be presented, followed by the theoretical approaches used to correlate the MEAM and experimental data. Finally, a discussion of the MEAM parameterization is presented, along with proposed applications for future work.

2. DENSITY FUNCTIONAL THEORY

Due to the absence of experimental data for SiAu, SiAg and AgAu alloys, one must resort to *ab initio* calculations to compute a sufficient number of properties for each system to correlate with the Modified Embedded Atom Method potentials. In this work, Density Functional Theory (DFT) was chosen to complete this task. In this chapter, a brief overview of DFT will be presented.

In order to predict the electronic and geometric structure of a cluster, molecule, gas or solid (henceforth referred to as the *system*) one must compute the total quantum mechanical energy of the system and subsequently minimize this energy with respect to its electronic and nuclear coordinates. Rather than attempt to find a single wavefunction which describes simultaneously the motion of electrons and nuclei, it is often sufficient to consider each system independently. There is a large difference in mass between electrons and nuclei, but the momentum of each particle is approximately equivalent. Consequently, the electrons respond nearly instantaneously to the motion of the nuclei[1]. Thusly, one may treat the nuclei adiabatically, resulting in a decoupling of the electronic and nuclear coordinates [51]. This simplification is known as the Born-Oppenheimer approximation [52]. The Born-Oppenheimer approximation reduces the many-body problem of electron-nuclei dynamics to that of dynamical electrons in some frozen configuration of nuclei. However, even with this simplification, the problem is still formidable.

[1]If the momenta, p, of electrons and nuclei are equal, and the masses satisfy the relation $m_n \ll m_e$, it follows that $v_e = p/m_e \gg v_n = p/m_n$.

To facilitate computation, one must further simplify the above many-body problem. Density Functional Theory, in principle, allows an exact mapping of a strongly interacting electron gas, in the presence of nuclei, onto that of a single particle moving in an effective nonlocal potential. In 1964, Hohenberg and Kohn proved that the total energy of an electron gas is a unique functional of electron density [53]. Further, they asserted that the minimum value of the total energy functional (a function of a function; ie. energy is a function of density, which itself is a function of position) is the ground-state energy of the system, and that the electron density which yields this minimum is the exact single-particle ground-state density. In the following year, Kohn and Sham described formally how to replace the many-electron problem by an equivalent set of self-consistent one-electron equations [54]. Combined, these two breakthroughs form the basis of modern density functional theory. As a result, an energy functional and a set of wavefunctions which minimize said functional were defined.

Consider a set of doubly occupied electronic states, ψ_i. The Kohn-Sham total-energy functional for this system is [50]:

$$E[\{\psi_i\}] = 2\sum_i \int \psi_i^* \left(-\frac{\hbar^2}{2m} \right) \nabla^2 \psi_i \, \mathrm{d}^3\mathrm{r} + \int V_{ion}(\mathrm{r}) n(\mathrm{r}) \, \mathrm{d}^3\mathrm{r} + \frac{e^2}{2} \int \frac{n(\mathrm{r}) n(\mathrm{r}')}{|\mathrm{r} - \mathrm{r}'|} \mathrm{d}^3\mathrm{r} \, \mathrm{d}^3\mathrm{r}' + E_{xc}[n(\mathrm{r})] + E_{ion}(\{\mathrm{R}_i\}) \tag{2.1}$$

where:

E_{ion} is the Coulomb energy associated with interactions amongst ions (or nuclei) at positions $\{\mathrm{R}_i\}$,

V_{ion} is the static total electron-ion potential,

$n(\mathrm{r}) = 2\sum_i |\psi_i|^2$ is the electron density, and

$E_{XC}[\,n(\mathrm{r})\,]$ is the exchange-correlation functional.

Physically, only the minimum of this functional has meaning; at its minimum, the Kohn-Sham energy functional equals the ground-state energy of the system of electrons with nuclei (or ions) at positions $\{\mathbf{R}_j\}$. In order to compute its minimum, a special set of wavefunctions, ψ_i, must be used. These wavefunctions are the eigenfunctions of the Kohn-Sham equation [50]:

$$\left[-\frac{\hbar^2}{2m}\nabla^2 + V_{ion}(\mathrm{r}) + V_H(\mathrm{r}) + V_{XC}(\mathrm{r})\right]\psi_i(\mathrm{r}) = \varepsilon_i\psi_i(\mathrm{r}) \tag{2.2}$$

where:

ψ_i is the wavefunction of electronic state i,

ε_i is the Kohn-Sham eigenvalue,

$V_H(\mathrm{r}) = e^2\int \frac{n(\mathrm{r}')}{|\mathrm{r}-\mathrm{r}'|}\mathrm{d}^3\,\mathrm{r}'$ is the Hartree potential of the electrons, and

$V_{XC}(\mathrm{r}) = \frac{\delta E_{XC}[n(\mathrm{r})]}{\delta n(\mathrm{r})}$ is the exchange-correlation potential.

The Kohn-Sham equation represents a mapping of an interacting many-electron system onto a system of noninteracting electrons moving in an effective potential due to the other electrons. Presently, the only term in the above equations which is not explicitly known is the exchange-correlation potential, V_{XC}. Should it become possible to define the exchange-correlation functional exactly, the functional derivative

with respect to density will produce an exchange-correlation potential that includes the effects of exchange and correlation exactly. In this case, the density functional theory result would be exact within the Born-Oppenheimer approximation. It is important to note that the sum of the single-particle Kohn-Sham eigenvalues does not give the total electronic energy: it overcounts the effects of electron-electron interaction in both the Hartree energy and the exchange-correlation energy. Hence, these eigenvalues are not strictly energies of single-particle electron states, but rather total energy derivatives with respect to the occupation numbers of these states. Nevertheless, the eigenvalue of the highest occupied eigenstate in an atomic (or molecular) calculation is quite nearly the ionization energy for that system.

In the subsequent sections, standard techniques to describe electron-electron, electron-ion and ion-ion interactions will be discussed, and accordingly each term in the Kohn-Sham energy functional and equation will be defined (cf. Equations 2.1 and 2.2).

2.1 Electron–Electron Interactions

In any electronic structure calculation, the most difficult problem is posed by the electron-electron interactions. Due to the Coulomb interaction between charges, the electrons repel one another. Hence, the Coulomb energy of a system of electrons may be reduced by spatially separating electrons, at the expense of increasing kinetic energy via deformations of the electronic wavefunctions.

As a consequence of the Pauli exclusion principle, the wavefunction of a many-electron system must be antisymmetric under exchange of any two electrons. This antisymmetry yields a spatial separation between electrons which have common spins, resulting in a reduction of the Coulomb energy of the system. This energy reduction due only to the antisymmetry of the wavefunction is known as the *exchange* energy. In a total energy calculation, methods which compute only the exchange energy (and neglect spatially separating opposite-spin electrons) will approach an energy minimum slightly higher than the true value. This limit is often referred to as the Hartree-Fock limit.

It is possible to reduce the Coulomb energy of an electronic system below the Hartree-Fock limit if one spatially separates opposite-spin electrons as well. In this case, the Coulomb energy of the system is reduced while the kinetic energy is increased; at a singular point the effect of decreasing the Coulomb energy and increasing the kinetic energy is balanced, and the true energy minimum is located. The energy difference between this minimum and the Hartree-Fock limit is called the *correlation* energy; it is extremely difficult to calculate in complex systems. Hence, this energy must be approximated (in general), and is the dominant source of discrepancy between *ab initio* computations and experimental results under the DFT formalism. In many published works, the exchange, E_x, and correlation, E_c, energies are grouped and called the *exchange-correlation* energy, $E_{xc} \equiv E_x + E_c$.

Many popular exchange-correlation functionals have a form appropriate for slowly varying densities. The most basic method to describe the exchange-correlation energy of an electronic system is known as the local density approximation (LDA). In this approximation, the exchange-correlation energy of the system is constructed

under the assumption that the exchange-correlation energy per electron at a point **r** in the electron gas, $\varepsilon_{xc}(\mathbf{r})$, is equal to the exchange-correlation energy per electron in a homogeneous electron gas, $\varepsilon_{xc}^{\text{hom}}$, that has the same density as the electron gas at point **r**. Mathematically, one might express the LDA as [55]:

$$E_{xc}^{\text{LDA}}[n(\mathrm{r})] = \int \varepsilon_{xc}^{\text{hom}}(\mathrm{r}) n(\mathrm{r}) \mathrm{d}^3\mathrm{r} \tag{2.3}$$

True to its name, the local density approximation assumes that the exchange-correlation energy functional is purely local; it ignores corrections to this energy at a point **r** due to nearby inhomogeneities in the electron density. However, this approximation remains popular as it yields a single well-defined global minimum for energy, allowing any energy minimization scheme to locate the global energy minimum for the system.

A logical improvement to the LDA is to include not only the electron density at a point r, but also its gradient. This approximation is known as the generalized gradient approximation (GGA). In general, GGA functionals have the form[55]:

$$E_{xc}^{\text{GGA}}\left[n(\mathrm{r})\right] = \int f\left[n(\mathrm{r}), \nabla n(\mathrm{r})\right] \mathrm{d}^3\mathrm{r} \tag{2.4}$$

In comparison with the local density approximation, the generalized gradient approximation tends to improve total energies [56], atomization energies [56 – 58], energy barriers and structural energy differences [59, 60]. It also tends to expand and soften bonds [58], which may [61] or may not [62] improve upon the local density approximation result. Unsurprisingly, the generalized gradient approximation is better suited for systems with highly inhomogeneous densities when compared to the local density approximation. In this work, the generalized gradient approxima-

tion of Perdew, Burke and Ernzerhof (PBE) [55] is used exclusively in our DFT calculations.

Once a suitable approximation for the exchange-correlation energy has been determined, one must next describe an infinite number of noninteracting electrons moving in a static potential of an infinite number of nuclei (or ions). Two challenges are presented in this scenario: first, as each electron requires its own wavefunction, an infinite number of wavefunctions are required to describe the system, and second, as each wavefunction extends over the entire solid, the basis set required to expand each is also infinite. Careful application of Bloch's theorem simultaneously provides a solution to both problems.

Bloch's theorem states that in a periodic solid, each electronic wavefunction may be decomposed into two constituent components, a cell-periodic term and a wave-like term [50]:

$$\psi_j(\mathbf{r}) = e^{i\mathbf{k}\cdot\mathbf{r}} f_j(\mathbf{r}) \tag{2.5}$$

The cell-periodic component may be expanded using a basis set of discrete plane waves whose wave vectors are the reciprocal lattice vectors of the crystal:

$$f_j(\mathbf{r}) = \sum_{\mathbf{G}} (c_{\mathbf{G}})_j \, e^{i\mathbf{G}\cdot\mathbf{r}} \tag{2.6}$$

where the c_j's are constant coefficients and the reciprocal lattice vectors, **G**, are defined by:

$$\mathbf{G}\cdot\mathbf{l} = 2\pi m \tag{2.7}$$

for all $\boldsymbol{l}$ where $\boldsymbol{l}$ is a real-space lattice vector of the crystal and m is an integer. Combining the above, each electronic wavefunction may now be expressed as a discrete sum of plane waves:

$$\psi_j(\mathbf{r}) = \sum_{\mathbf{G}} (c_{\mathbf{k}+\mathbf{G}})_j \, e^{i(\mathbf{k}+\mathbf{G})\mathbf{r}} \tag{2.8}$$

Discretizing the electronic wavefunctions alters the problem of calculating an infinite number of wavefunctions to one of calculating a finite number of wavefunctions at an infinite number of points in reciprocal space (herein k-points and k-space, respectively). In theory, electrons occupying states at each k-point contribute to the electronic potential in the bulk solid and so an infinite number of k-point calculations are required to compute the potential. In practice, however, the electronic wavefunctions at k-points that are spatially nearby will be approximately equivalent; it is possible to represent wavefunctions over a region of k-space by a single, properly weighted wavefunction at one k-point. Therefore, only a finite number of k-points are required to calculate the electronic potential (and thus the total energy) of the solid. Several schemes exist for defining the k-point grid [63 – 67]. In the DFT calculations performed in this work, the Monkhorst-Pack scheme [65] was used exclusively.

Finally, one must consider the sum over reciprocal lattice vectors, **G**, in the Bloch expansion of electronic wavefunctions. Once again, the theory implies that this sum be infinite. In practice, however, the coefficients c_j become vanishingly small for plane waves with large kinetic energy. Consequently, by introducing a cut-off energy, the plane wave basis may be truncated to include contributions only from plane waves with a kinetic energy less than the cut-off. Thus, the infinite basis set be-

comes finite. Two problems arise when using an energy cut-off: first, changes in the unit cell size and shape create discontinuities in the plane wave basis, and second, the number of basis states change discontinuously with cut-off energy (additionally, for a given k-point set, k-point occupation changes with varying cut-off energy). Modern techniques are used to remedy these problems by applying correction factors which account for the difference between the number of states in a basis set with an infinitely large number of k-points and the number of k-points actually used in the calculation [68].

Once all of these approximations have been made, the Kohn-Sham equations assume a simple form [50]:

$$\sum_{G'}\left[\frac{\hbar^2}{2m}|\mathrm{k}+\mathrm{G}|^2\delta_{GG'}+V_{ion}(\mathrm{G}-\mathrm{G}')+V_H(\mathrm{G}-\mathrm{G}')+V_{XC}(\mathrm{G}-\mathrm{G}')\right](c_{\mathrm{k}+G'})_i=\varepsilon_i(c_{\mathrm{k}+G})_i \quad (2.9)$$

In this form, the kinetic energy is diagonal (as indicated by $\delta_{GG'}$), and the potentials are all described in terms of their Fourier Transforms. The solution proceeds by disagonalizing the Hamiltonian matrix, whose elements are given in the square brackets above. The size of this matrix is determined by the cut-off energy and may be extremely large for systems which contain both core and valence electrons. To overcome this, a psendopotential approximation, as described in the next section, is employed. Finally, one should note that non-periodic systems are slightly more complex. For a detailed treatment of non-periodic systems, the reader is referred to reference [50].

2.2 Electron–Ion Interactions

To perform an all-electron calculation, an extremely large plane wave basis set is required both to expand the tightly-bound core orbitals, and to follow the rapid oscillations necessary to maintain orthogonality (required by the Pauli exclusion principle) of the (valence) electrons in the core region. Many chemical and physical properties have a much greater dependence on the valence electrons, rather than the core electrons. The pseudopotential approximation exploits this by removing the core electrons and replacing them (and their strong ionic potential) by a weaker pseudopotential that acts on a set of pseudo-wavefunctions rather than the true valence wavefunctions. Ideally, this pseudopotential is constructed to maintain the scattering properties and phase shifts of the ion and core electrons for the valence wavefunctions, but in such a way that the pseudo-wavefunctions have no radial nodes in the core region, thereby eliminating oscillations. Outside of the core region, the core potential and pseudopotential are identical, and the scattering from either indistinguishable.

For each angular momentum component of the valence wavefunction, a different phase shift is produced by the ion core. Similarly, scattering from a pseudopotential must also be a function of angular momentum. In its most general form, the (nonlocal) pseudopotential is expressed as [50]:

$$V_{NL} = \sum_{lm} |lm\rangle V_l \langle lm| \tag{2.10}$$

where $|lm\rangle$ are the spherical harmonics and V_l is the pseudopotential for angular momentum l. When acting on the electronic wavefunctions, this operator decom-

poses the wavefunction into spherical harmonics, each of which is multiplied by the relevant pseudopotential. A *local* pseudopotential is one which is a function only of the distance from the nucleus; it uses the same potential for all angular momentum components of the wavefunction. Conversely, a *nonlocal* pseudopotential is one which has a unique potential for each angular momentum component of the wavefunction.

As shown in the previous section, total energy calculations of an electronic system are a function of electronic density. In order for the exchange-correlation energy to be determined accurately, it is imperative that outside of the core regions the pseudo-wavefunctions and real wavefunctions be identical, not only in spatial dependencies but also in absolute magnitudes so that the two wavefunctions generate equivalent charge densities. To accomplish this, the pseudopotential must be adjusted such that the integrals of the squared-amplitudes of the real and pseudo-wavefunctions inside the core regions are identical. Psuedopotentials which have undergone this adjustment are known as *norm conserving* pseudopotentials. Modern pseudopotentials also have the ability to describe scattering due to the ion in a variety of valence configurations, a property known as *transferability*.

Besides the obvious advantage of computing fewer electronic wavefunctions due to the removal of core electrons, there are other compelling reasons to consider pseudopotential calculations over all-electron calculations. First, as previously mentioned, the electronic wavefunctions may be expanded using far less plane wave basis states when compared to the all electron potential, as oscillations have been eliminated. This results in a reduction of the size of the Hamiltonian matrix, and a more efficient computation. The second, and less obvious, advantage is that one

requires less numerical precision in a pseudopotential calculation when compared to the equivalent all-electron calculation. The difference between electronic energies of different ionic configurations is observed almost entirely in the energy of the valence electrons alone. The total energy of the valence electron system is on the order of one-thousand times smaller than the total energy of the equivalent all-electron system, and yet the energy differences between ionic configurations remains the same for either computation. Any rounding and step-size errors accumulated when summing contributions from the core electrons in an all-electron calculation will overshadow these small energy differences, a problem which is eliminated completely in the pseudopotential regime. One should note, however, that total energy is no longer meaningful in pseudopotential calculations; only energy differences are significant.

To obtain the static total ionic potential, V_{ion}, in a solid, one places an ionic pseudopotential at the position of every nuclei in the solid. Information regarding the positions of ions is contained in the structure factor, which for ions of species α at wave vector $\mathbf{G}$ has the value [50]:

$$S_\alpha(\mathbf{G}) = \sum_I e^{i\mathbf{G}\cdot\mathbf{R}_I} \tag{2.11}$$

where the sum is over the positions $\mathbf{R}_I$ of all the ions of species α in a single unit cell. The periodicity of the system restricts nonzero components of the ionic potential to its reciprocal lattice vectors; it is necessary only to compute the structure factor at the set of these vectors. The total ionic potential is thus obtained by summing the product of the structure factor and the pseudopotential over each species of ion. For instance, for a local potential, v_α, V_{ion} is defined simply as [50]:

$$V_{ion}(\mathbf{G}) \quad \sum_{\alpha} S_{\alpha}(\mathbf{G}) v_{\alpha}(\mathbf{G}) \tag{2.12}$$

Away from the core, an ideal pseudopotential is purely Coulombic, of the form $Z/\mathbf{R}$, where Z is the valence of the atom. Upon taking the Fourier Transform, the ideal pseudopotential diverges as $Z/\mathbf{G}^2$ at small wave vectors. Hence, the total ionic potential at $\mathbf{G} = 0$ is infinite, and so the electron-ion energy is infinite. However, similar divergences are observed in the Coulomb energies due to the electron-electron and ion-ion interactions. When combined, the total Coulomb energy at $\mathbf{G} = 0$ for all three interactions cancel exactly; this must be the case as the Coulomb potential for a charge-neutral system at $\mathbf{G} = 0$ is zero [50]. Without loss of generality, the $\mathbf{G} = 0$ term for each type of interaction is set to zero. One should note that typical pseudopotentials are not purely Coulombic; corrections for the contribution to total energy arising due to this discrepancy must be made [50].

Many methods exist to generate pseudopotentials [69 – 71]. In this work, pseudopotentials were generated using the RRKJ (Rappe, Rabe, Kaxiras and Joannopoulos) method [69]. This method is unique in that it applies an additional optimization step after generating an initial pseudopotential to set the cut-off energy to a desired target.

2.3 Ion–Ion Interactions

The Coulomb interaction between ions is extremely difficult to calculate, as it is long-ranged in both real space and reciprocal space. Ewald developed a rapidly converging method to perform Coulomb summations over periodic lattices based

on the identity [50]:

$$\sum_{l}\frac{1}{\left|\mathbf{R}_1+l-\mathbf{R}_2\right|}=\frac{2}{\sqrt{\pi}}\sum_{l}\int_{\eta}^{\infty}e^{-\left|\mathbf{R}_1+l-\mathbf{R}_2\right|^2\rho^2}\,d\rho+\frac{2\pi}{\Omega}\sum_{\mathbf{G}}\int_{0}^{\eta}e^{-\frac{|\mathbf{G}|^2}{4\rho^2}+i(\mathbf{R}_1-\mathbf{R}_2)\cdot\mathbf{G}}\frac{d\rho}{\rho^3} \qquad (2.13)$$

where l are lattice vectors, $\mathbf{G}$ are reciprocal lattice vectors and Ω is the unit cell volume. With this identity, it is possible to express the lattice summation for Coulomb energy due to the interaction between an ion positioned at $\mathbf{R}_2$ and an array of atoms at positions $\mathbf{R}_1+l$. At first glance, it appears that replacing the infinite Coulomb summation on the left-hand side of the equation by two infinite summations (one over real space vectors, the other over reciprocal space vectors) on the right-hand side would only serve to complicate things. However, with the appropriate choice of η, the two infinite summations converge rapidly in their respective spaces. In practice, the real and reciprocal space summations can be computed using only a few vectors in each space.

As in the previous section, the $\mathbf{G}=0$ contribution must be removed to compute the correct total energy. Unlike in the previous section, the $\mathbf{G}=0$ contribution is now divided between the real and reciprocal space summations; it is not sufficient to only eliminate this term in the reciprocal space Ewald summation. Once the appropriate corrections have been made, the correct form for the total ion energy, E_{ion}, is [50]:

$$E_{ion}=\frac{1}{2}\sum_{i,j}Z_iZ_je^2\left[\sum_{l}\frac{\operatorname{erfc}\left(\eta\left|\mathbf{R}_1+l-\mathbf{R}_2\right|\right)}{\left|\mathbf{R}_1+l-\mathbf{R}_2\right|}-\frac{2\eta}{\sqrt{\pi}}\delta_{ij}\right.$$
$$\left.+\frac{4\pi}{\Omega}\sum_{\mathbf{G}\neq0}\frac{1}{|\mathbf{G}|^2}e^{-\frac{|\mathbf{G}|^2}{4\eta^2}}\cos\left[(\mathbf{R}_1-\mathbf{R}_2)\cdot\mathbf{G}\right]-\frac{\pi}{\eta^2\Omega}\right] \qquad (2.14)$$

where Z_I and Z_J are the valences of ions I and J respectively, and **erfc** is the compliMentary error function:

$$\mathrm{erfc}(z) = \frac{2}{\sqrt{\pi}} \int_{z}^{\infty} e^{-t^2} dt \qquad (2.15)$$

Note that an ion does not interact with its own Coulomb charge, so the $I=0$ term must be omitted from the real space summation when $I=J$.

This concludes the discussion of Density Functional Theory. In the next chapter, the theory of the Modified Embedded Atom Method (MEAM) will be presented.

3. The Modified Embedded Atom Method

3.1 The Embedded Atom Method

Before one can properly define the Modified Embedded Atom Method (MEAM), it is necessary to first define the Embedded Atom Method (EAM). The EAM utilizes the electron density to compute the total energy of a system. It has the ability to realistically treat impurities, defects and other complex systems, while being not significantly more complicated to use than pair-potentials which can describe neither. In the previous section, it was shown that energy is a functional of electron density, and that potential is determined to within an additive constant by a system's electron density. The EAM is based on a useful corollary to the Hohenberg-Kohn formalism by Stott and Zaremba: the energy of an impurity in a host is a functional of the electron density of the unperturbed (ie. without impurity) host [72]:

$$E = \mathcal{F}_{Z,\mathbf{R}}\left[n_H\right] \tag{3.1}$$

where $n_H(\mathbf{R})$ is the electron density of the unperturbed host and Z and $\mathbf{R}$ are the type and position of the impurity respectively. Thus, under this corollary, the embedding energy of an impurity is determined by the electron density of the host before the impurity is added. In the EAM, each atom in a system is considered to be

an impurity in a host consisting of all the other atoms. Specifically, the embedding energy, E_i, is defined to be the energy of an atom in an uniform electron gas relative to the energy of the atom when separated from the electron gas.

The functional $\mathcal{F}$ is a universal function, independent of the host. Its exact form is unknown and is likely complicated, but in the EAM a simple approximation assumes that the embedding energy depends only on the environment in the immediate vicinity of the impurity. Analogous to the local density approximation in DFT, each impurity experiences a locally uniform electron density. With this approximation, the per-atom energy in the EAM formalism is given by [73]:

$$E_i = F_i\left(n_i\right) + \frac{1}{2}\sum_j \varphi\left(\mathrm{R}_{ij}\right) \tag{3.2}$$

where the functional $\mathcal{F}$ is approximated by a functional, F_i of the electron density (without atom i), n_i, at the impurity site and a short-range electrostatic pair potential, ϕ, has also been added to account for core-core repulsion between atoms i and j separated by a distance $\mathbf{R}_{ij}$. The total energy is merely the sum over all individual contributions [73]:

$$E_{\mathrm{tot}} = \sum_i F_i\left(n_{H,i}\right) + \frac{1}{2}\sum_{i,j} \varphi\left(\mathrm{R}_{ij}\right) \tag{3.3}$$

It is of crucial importance to note that the embedding functional, F_i is not trivially related to the functional $\mathcal{F}$. In terms of the functional, $\mathcal{F}$, the energy required to remove an atom from the solid, leaving a vacancy (and neglecting any lattice relaxations) is given by [74]:

$$E = \mathcal{F}_{\mathrm{atom}}\left[n_{\mathrm{solid}}(\mathrm{r})\right] \tag{3.1}$$

where n_{solid} is the density of the solid including the vacancy. It must also be true that the same energy be obtained by viewing the solid with the vacancy as an impurity and the single atoms as the host so that [71]:

$$E = \mathcal{F}_{solid}\left[n_{atom}(\mathbf{r}) \right] \tag{3.5}$$

In terms of the embedding functional, F, the expression for total energy (Equation 3.3) reduces to [74]:

$$E = \sum_{i} \left[F_i\left(n_i^*\right) - F_i\left(n_i\right) \right] \tag{3.6}$$

where the sum is over all atoms except the one removed and n_i is the electronic density at atom i in the solid with the vacancy. Each of the energies in Equations 3.4, 3.5 and 3.6 must be equal, and consequently the relationship between $\mathcal{F}$ and F is nontrivial.

A final simplification assumes that the host electron density, $n_H(\mathbf{R})$, is closely approximated by a linear superposition of the atomic densities, n^a, of the constituents [74]:

$$n_{H,i} = \overline{n}_i = \sum_{\substack{j \\ (\neq i)}} n_j^a\left(\mathbf{R}_{ij}\right) \tag{3.7}$$

With this approximation, energy is simply a function of the position of the atoms. Up to this point, all parameters in the EAM energy have been explicitly defined. However, the EAM is a semi-empirical potential; the functions F and ϕ must be empirically determined by fitting the potential to experimental data.

3.2 THE MODIFIED EMBEDDED ATOM METHOD

In the previous section, the fundamental theory of the Embedded Atom Method was discussed. The EAM has successfully been used to describe FCC, BCC and other nearly-filled *d*-band metals, but has proven ineffective at describing covalent systems such as silicon and germanium [38]. The first modifications to the EAM redefined the electron density, $\overline{n}_i$, to describe directional bonding specifically in silicon [75]. Formally, the Modified Embedded Atom was introduced as a generally applicable potential in a paper describing its application to the silicon-germanium system [36]. In what follows, the modifications to the EAM will be discussed.

Equation 3.3 presents the total energy as formulated in the EAM. As defined previously, F_i is the embedding functional which defines the energy required to embed an atom of type i into a background electron density $\overline{n}_i$ at site i and ϕ_{ij} is a pair interaction between atoms i and j separated by a distance $\mathbf{R}_{ij}$. In the EAM, ϕ_{ij} was assumed to be entirely repulsive, but it was realized that the nonuniqueness of F_i and ϕ_{ij} allows more general forms of ϕ_{ij}. Also, in the EAM the electron density, $\overline{n}_i$, is given by a linear superposition of spherically-averaged atomic electron densities (cf. Equation 3.7); in the MEAM, $\overline{n}_i$ is augmented by additional angular-dependent terms. The energy per atom in the MEAM is defined as in the EAM, that is [38]:

$$E_i = F_i\left(\frac{\overline{n}_i}{Z_i}\right) + \frac{1}{2}\sum_{j\,(j\neq i)} \varphi_{ij}\left(\mathrm{R}_{ij}\right) \tag{3.8}$$

where, without loss of generality, the background density, $\overline{n}_i$, has been renormalized by the number of nearest neighbours, Z_i, which is defined as the *reference structure* for an atom of type i by Baskes [38]. This reference structure is a crystal structure

which contains detailed information about the behaviour of atom i and is usually, but not always, the equilibrium crystal structure of type i atoms. Note that while this expression is indeed similar to the energy expression in the EAM (cf. Equation 3.2), its constituent functions F, $\overline{n}$ and ϕ_{ij} are in fact quite different. In the reference structure for an atom of type i, the per atom energy, E_i^u, of the reference structure as a function of the nearest neighbour distance is expressed as [38]:

$$E_i^u(\mathrm{R}) = F_i\left(\frac{\overline{n}_i^0(\mathrm{R})}{Z_i}\right) + \frac{Z_i}{2}\sum_{\substack{j \\ i \neq j}} \varphi_{ij}(\mathrm{R}) \tag{3.9}$$

where $\overline{n}_i^0(\mathbf{R})$ is the background electron density for the reference structure of atoms of type i and $\mathbf{R}$ is the nearest neighbour distance in this configuration. Assuming E_i^u is known, the above expression can be used to determine the pair interaction for type i atoms as [38]:

$$\varphi_{ii}(\mathrm{R}) = \frac{2}{Z_i}\left(E_i^u(\mathrm{R}) - F_i\left(\frac{\overline{n}_i^0(\mathrm{R})}{Z_i}\right)\right) \tag{3.10}$$

If the pair interaction is assumed to take this form, Equation 3.8 for a monatomic system may be rewritten as:

$$E_i = \frac{1}{Z_i}\sum_{\substack{j \\ i \neq j}} E_i^u\left(\mathrm{R}_{ij}\right) + F_i\left(\frac{\overline{n}_i}{Z_i}\right) - \frac{1}{Z_i}\sum_{\substack{j \\ i \neq j}} F_i\left(\frac{\overline{n}_i^0\left(\mathrm{R}_{ij}\right)}{Z_i}\right) \tag{3.11}$$

Physically, the first term in the Equation 3.11 represents the average of the per atom energy of the reference lattice at each of the nearest neighbour distances. The last two terms are formed by the difference between the embedding energy at the background electron density actually seen by atom i and the average embedding energy of this atom in the reference lattice at each of the nearest neighbour distances respectively. Essentially, these two terms form a new kind of embedding

energy where the embedding reference state is that of the reference lattice rather than isolated atoms.

Additionally, in the B1 (NaCl) structure considered for SiAg, SiAu and AuAg systems, the pair interaction takes the form [40]:

$$\varphi_{\eta}(\mathrm{R}) = \frac{1}{Z_{\eta}}\left(2E_{\eta}^{u}(\mathrm{R}) - F_{i}\left(\overline{n}_{i}^{0}\right) - F_{j}\left(\overline{n}_{i}^{0}\right)\right) \tag{3.12}$$

where Z_{η} is the number of nearest neighbours in the B1 structure, and the embedding energies, F, and background electron densities, $\overline{n}^{0}$, are as evaluated in the monatomic reference structures. Equation 3.8 then becomes:

$$E_{i} = \sum_{j \neq i} \frac{E_{ij}^{u}(\mathrm{R})}{Z_{ij}} + F_{i}\left(\frac{\overline{n}_{i}}{Z_{i}}\right) \quad \frac{1}{2}\sum_{j \neq i} \frac{F_{i}\left(\overline{n}_{i}^{0}\right) + F_{j}\left(\overline{n}_{i}^{0}\right)}{Z_{\eta}} \tag{3.13}$$

whose terms are analogous to those described in Equation 3.11.

As in the EAM, the MEAM limits interactions to first nearest neighbours only. This limitation introduces important questions about cut-offs and screening. There are two basic schemes which allow one to artificially limit interactions between atoms. The first scheme forces all distance dependent functions to zero smoothly at a predetermined cut-off distance, implemented by multiplying distance dependent functions by a "cut-off" function which smoothly goes from unity to zero as a function of increasing distance. The second approach, as used in the MEAM, is slightly more complex. In this scheme, a screening method between an atom and its nearest neighbours is used which reduces the effect of interactions of any atoms which are not nearest neighbours. This scheme takes into account the actual geometry of the atoms under consideration, and is therefore much more robust than a simple

cut-off function. For instance, with the screening method, planar type structures, such as HCP and graphene, naturally interact with more distant out-of-plane atoms even though the in-plane atoms are much nearer. Similarly, atoms approaching free surfaces interact with the surface atoms at distances much greater than the in-plane nearest neighbours. In any such case, the interactions between distant, unscreened atoms are governed not by an arbitrary cut-off distance, but rather by the unscreened electron density itself. In the MEAM, this screening function takes the form [38, 40]:

$$S_{ik} = \prod_{\substack{j \\ j \neq i,k}} S_{ijk} \tag{3.14}$$

where

$$S_{ijk} = \begin{cases} 0, & C \leq C_{\min} \\ \left[1 - \left(\dfrac{C_{\max} - C}{C_{\max} - C_{\min}} \right)^4 \right]^2, & C_{\min} < C < C_{\max} \\ 1, & C \geq C_{\max} \end{cases} \tag{3.15}$$

and

$$C = 1 + 2\frac{\mathrm{R}_{ij}^2\,\mathrm{R}_{ji}^2 + \mathrm{R}_{ki}^2\,\mathrm{R}_{ji}^2 - \mathrm{R}_{jk}^4}{\mathrm{R}_{jk}^4 - \left(\mathrm{R}_{ij}^2 - \mathrm{R}_{ki}^2\right)^2} \tag{3.16}$$

In Equation 3.15, $C_{\max}$ and $C_{\min}$ are adjustable parameters chosen to limit the range of atomic interactions to first nearest neighbours. Consider the screening between atoms i and k by atom j, as shown schematically in Figure 3.1. Suppose atoms i and j are nearest neighbours, with touching atomic spheres. If atom k lies within the screened cone (blue area) defined by i, j and the parameter $C_{\min}$ (typically, this cone

angle is on the order of 30°), it may be considered completely screened from atom i. Similarly, if atom k lies in the red region defined by by i, j and the parameters C_{min} and C_{max} (typically, the larger cone angle is on the order of 60°) it may be considered partially screened from atom i, the amount of which depends on both the distance and the angle between the atoms. Finally, if atom k lies beyond the region defined by C_{max} (green area), it is considered completely unscreened by atom j.

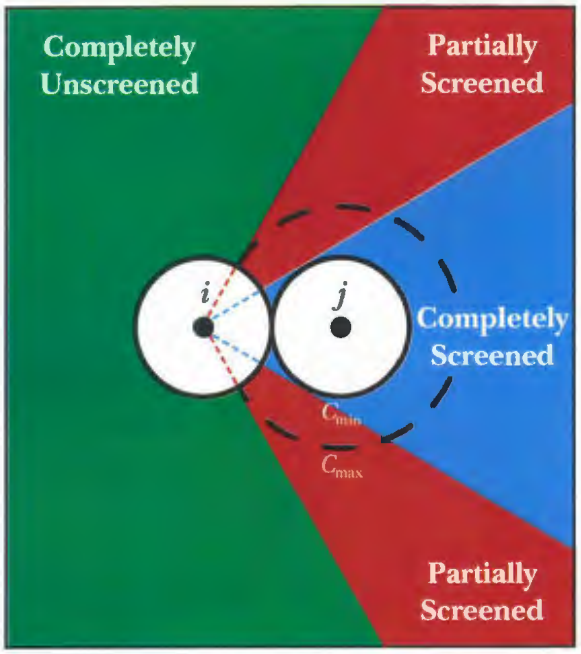

Figure 1: Schematic representation of the screening function, S_{ik}.

With a suitably defined screening function, one may now discuss in detail the components of Equations 3.11 and 3.13. To begin, one must first decide how to compute the background electron density. As discussed previously, the EAM computes the background electron density as a linear superposition of the spherically averaged electron densities of the constituent atoms. In the MEAM, this component is the dominant contribution to a series of partial electron densities, the first of which is [38, 40]:

$$n_i^{(0)} = \sum_{\substack{j \\ j \neq i}} n_j^{a(0)}\left(S_{ij}\right) \tag{3.17}$$

where $n_j^{a(0)}$ represents the atomic electron density of a type j atom at a (suitably screened) distance S_{ij} from site i. Note that Equations 3.7 (EAM) and 3.17 (MEAM) are identical, as expected. Equation 3.17, however, is further generalized by a series of correction electron densities that explicitly depend on the relative positions of the neighbours of atom i [38, 40, 76]:

$$\left(n_i^{(1)}\right)^2 = \sum_{\alpha}\left(\sum_{\substack{j \\ j \neq i}} x_{ij}^{\alpha} n_j^{a(1)}\left(S_{ij}\right)\right)^2 \tag{3.18}$$

$$\left(n_i^{(2)}\right)^2 = \sum_{\alpha,\beta}\left(\sum_{\substack{j \\ j \neq i}} x_{ij}^{\alpha} x_{ij}^{\beta} n_j^{a(2)}\left(S_{ij}\right)\right)^2 - \frac{1}{3}\left(\sum_{\substack{j \\ j \neq i}} n_j^{a(2)}\left(S_{ij}\right)\right)^2 \tag{3.19}$$

$$\left(n_i^{(3)}\right)^2 = \sum_{\alpha,\beta,\gamma}\left(\sum_{\substack{j \\ j \neq i}} x_{ij}^{\alpha} x_{ij}^{\beta} x_{ij}^{\gamma} n_j^{a(3)}\left(S_{ij}\right)\right)^2 \tag{3.20}$$

where

$$n_j^{a(l)}(\mathrm{R}) = n_j^0 \, \mathrm{e}^{-\beta_j^{(l)}\left(\frac{\mathrm{R}}{\mathrm{R}_e} - 1\right)} \tag{3.21}$$

are atomic electron densities with adjustable decay constant $\beta_j^{(l)}$ for atom j, and

$$x_{ij}^{\alpha} = \frac{\mathrm{R}_{ij}^{\alpha}}{\mathrm{R}_{ij}} \tag{3.22}$$

with $\mathbf{R}_{ij}^{\alpha}$ being the α-component of the distance vector between atoms j and i. The

form of Equations 3.18, 3.19 and 3.20 are chosen such that the partial background electron densities are invarient to both lattice translation and rotation, scale with atomic electron density for homogeneous deformation and equal zero for a cubic lattice with a center of symmetry. It has been shown that Equations 3.18, 3.19 and 3.20 are equivalent to the three-body cos, $\cos^2$ and $\cos^3$ dependences commonly observed in many-body potentials, respectively [38]. For instance, Equation 3.18 may be expressed equivalently as [38]:

$$\left(n_i^{(1)}\right)^2 = \sum_{\substack{j,k \\ i \neq j,k}} n_j^{a(1)}\left(S_{ij}\right) n_k^{a(1)}\left(S_{ik}\right) \cos\left(\theta_{jik}\right) \tag{3.23}$$

where θ_{jik} is the angle between atoms j, i and k. Considering the geometric way that the densities $n_j^{(l)}$ are defined, one may consider each to be related to a specific angular momentum contribution (s,p,d and f respectively) to the background electron density, and that the associated atomic electron densities are related to averages of these densities. It remains to combine the contributions of each partial electron density to form a total density which is to be used as the argument of the embedding function. As in DFT, this scalar must represent electron density throughout all space. Linear superposition appears, at first, to be the obvious choice, but the square root necessary to solve Equations 3.18, 3.19 and 3.20 introduces singularities into the resultant density (and hence, energy). Instead, the total background density is constructed by taking a weighted sum of the squares of the partial background densities [38]:

$$\left(\overline{n}_i\right)^2 = \sum_{l=0}^{3} t_i^{(l)} \left(n_i^{(l)}\right)^2 \tag{3.24}$$

where $t_i^{(l)}$ are adjustable weighting functions for the partial electron densities, and $t_i^{(0)}$ is, without loss of generality, unity. Equation 3.24 may alternatively be viewed as a perturbative expansion of the background density about the linear superposition $n_i^{(0)}$ [38]:

$$\overline{n}_i = n_i^{(0)}\left(1+\frac{1}{2}\sum_{l=1}^{3} t_i^{(l)}\left(\frac{n_i^{(l)}}{n_i^{(0)}}\right)^2+\ldots\right) \tag{3.25}$$

where the correction terms $l=1,2,3$ may be physically thought of as adjustments to the spherical density due to the existence of density gradients, divergences or losses of inversion symmetries respectively. One final simplification may be made to the background density should the geometry of the system in question be known. If this is the case, the sum over atoms j in Equations 3.17, 3.18, 3.19 and 3.20 may be computed, and the final background electron densities take the form [40]:

$$\overline{n}_i = \begin{cases} \dfrac{n_i^{(0)}}{n_i^0}\dfrac{2}{1+e^{-1}}, & \text{Si} \\ \dfrac{n_i^{(0)}}{n_i^0}\sqrt{1+\Gamma_i}, & \text{Ag, Au} \end{cases} \tag{3.26}$$

with

$$\Gamma_i = \sum_l t_i^{(l)}\left(\frac{n_i^{(l)}}{n_i^{(0)}}\right) \tag{3.27}$$

where Γ_i is the term describing the angular dependence ($l=0,1,2,3$ corresponds to s,p,d,f symmetry respectively) $n_i^{(l)}$ are the partial electron densities, and n_i^0 is the composition-dependent electron density scaling factor for atom i.

The next component of interest in Equations 3.11 and 3.13 is the per atom energy, E_i^u. To compute this value, the Rose equation of state is used [77]:

$$E_i^u(\mathrm{R}) = -E_i^0\left[1 + a - \left(\mathrm{att} - \frac{\mathrm{rep}}{\mathrm{R}}\right)a^3\right]e^{-a} \tag{3.28}$$

where **att** and **rep** are adjustable parameters, not shown in the universal equation of state, necessary to adjust the attractive and repulsive energies in the MEAM potential to fit *ab initio* calculations. The parameter a is defined as [38]:

$$a = \alpha_i\left(\frac{\mathrm{R}}{\mathrm{R}_i^0} - 1\right) \tag{3.29}$$

and

$$\begin{aligned} \alpha_i &= \sqrt{\frac{9B_i\Omega_i}{E_i^0}} \\ &= \sqrt{\frac{K_i}{E_i^0}}\,\mathrm{R}_i^0 \end{aligned} \tag{3.30}$$

where $\mathbf{R}_i^0$ is the equilibrium nearest neighbour distance and B_i is the bulk modulus, Ω_i is the atomic volume for the solid phase, K_i is the diatomic force constant for the gas phase, and E_i^0 is the cohesive energy for type i atoms in the reference structure. Near equilibrium, E_i^u is extremely well-defined as it is computed directly from experimental data. Away from equilibrium, it depends entirely upon the equation of state, which behaves reasonably for a>-1 [77].

The final component of Equations 3.11 and 3.13 is the embedding function, F_i. It is defined to be a simple function of the electron density [38]:

$$F_i(n) = A_i E_i^0 n \ln(n) \tag{3.31}$$

where A_i is yet another parameter to be determined. The logarithmic dependence was chosen as to provide the correct correlation between bond length and energy [36].

Table 3.1: Summary of the parameters to be determined in the MEAM potential.

PARAM	DESCRIPTION	PROCEDURE
E_i^0	cohesive energy	direct from experimental data
$\mathbf{R}_i^0$	equilibrium nearest neighbour distance	direct from experimental data
α_i	exponential decay factor for rose equation of state	equation 3.30 provided **att** and **rep** small; variational method otherwise
n_i^0	composition-dependent electron density scaling factor for partial electron densities	unity for monatomic systems; variational method otherwise
A_i	scaling factor for embedding energy	variational method
$\beta_i^{(0)}$	exponential decay factor for partial electron density $n_i^{(0)}$	variational method
$\beta_i^{(1)}$	exponential decay factor for partial electron density $n_i^{(1)}$	variational method
$\beta_i^{(2)}$	exponential decay factor for partial electron density $n_i^{(2)}$	variational method
$\beta_i^{(3)}$	exponential decay factor for partial electron density $n_i^{(3)}$	variational method
$t_i^{(0)}$	weighting factor for partial electron density $n_i^{(0)}$	unity
$t_i^{(1)}$	weighting factor for partial electron density $n_i^{(1)}$	variational method
$t_i^{(2)}$	weighting factor for partial electron density $n_i^{(2)}$	variational method
$t_i^{(3)}$	weighting factor for partial electron density $n_i^{(3)}$	variational method
att	attractive adjustment for rose equation of state	variational method
rep	repulsive adjustment for rose equation of state	variational method
$C_{\min}$	adjustable parameter in screening factor	variational method
$C_{\max}$	adjustable parameter in screening factor	variational method

A summary of the parameters required to create a functional MEAM potential is provided in Table 3.1. In early applications of the MEAM, attempts were made to define each unknown parameter as a function of a known experimental quantity (or quantities; see, for instance, [38]). Two problems exist with this approach. First, several of the parameters (eg. $\beta_i^{(1)}$, $\beta_i^{(2)}$, $\beta_i^{(3)}$, A_i, **att** and **rep**) appear unable to be related directly to an experimental quantity. Second, the equations which do exist to relate parameters to known quantities are true only in the specific case of A_i equal to unity and **att** and **rep** equal to zero. Due to these limitations, and a marked increase in computing power, modern fit techniques use a completely variational approach (see, for example, [37, 39, 40, 78]). In this work, a variational method is adopted to determine all unknown parameters. In the next chapter, the experimental data used to characterize the MEAM potential parameterization is presented.

4. MEAM Parameterization

To determine the parameters in Table 3.1, a variety of thermoelastic, structural, point defect and surface properties are computed theoretically and compared directly to their experimental values. In this chapter, the theoretical methods to calculate each property are described. To begin, the thermoelastic properties will be discussed.

4.1 Thermoelastic Properties

To compute the static structural properties, such as the lattice constant, cohesive energy and bulk modulus of a system, it is sufficient to consider total energy as a function of volume for the reference structure. The equilibrium lattice constant is thus defined by the volume at which the total energy is minimized; correspondingly, the cohesive energy is this minimum energy per atom in the system.

To determine the bulk modulus and its pressure derivative, one must compute energy as a function of volume and subsequently fit this data to an equation of state. As the fit procedure is fully automated, erroneous fit parameters may be reported if the data is discontinuous or noisy. For this reason, two equations of state are considered which, at absolute zero, are equivalent. These equations of state are known as the Murnaghan equation of state [79, 80] and the Birch-Murnaghan third-order

isothermal equation of state [81]. In the event that the parameters derived from each curve fit differ by more than 2.5%, the MEAM parameter set is disregarded. If the fit parameters fall within this tolerance, the data is assumed to be continuous and the fit appropriate.

The Murnaghan equation of state is based upon the assumption that the bulk modulus of a solid compressed to a finite strain with respect to pressure behaves linearly. For a fixed number of particles at a temperature of absolute zero, pressure and volume are related by the expression [79]:

$$P(V) = \frac{B_0}{B_0'}\left[\left(\frac{V_0}{V}\right)^{B_0'} - 1\right] \tag{4.1}$$

where

$$B_0' = \left(\frac{\partial B_0}{\partial P_0}\right)_T \tag{4.2}$$

and B_0, V_0 and P_0 are the equilibrium bulk modulus, volume and pressure respectively. Furthermore, at absolute zero, pressure is assumed to be a function of volume only [79]:

$$P(V) = -\frac{dE(V)}{dV} \tag{4.3}$$

By equating 4.1 and 4.3 and integrating, one obtains an expression for energy as a function of volume, known as the Murnaghan equation of state [79]:

$$E(V) = \frac{B_0 V}{B_0'}\left[\frac{1}{B_0'-1}\left(\frac{V_0}{V}\right)^{B_0'} + 1\right] + C \tag{4.4}$$

where C is a constant of integration:

$$C = E_0 - \frac{B_0 V_0}{B_0' - 1} \tag{4.5}$$

It has been shown that Equation 4.4 is not well-behaved when using standard non-linear least-squares fitting routines [80]. Hence, to facilitate curve-fitting, Equations 4.4 and 4.5 may be re-written as [80]:

$$E(V) = \frac{B_0 V}{B_0'(B_0' - 1)}\left[B_0'\left(1 - \frac{V_0}{V}\right) + \left(\frac{V_0}{V}\right)^{B_0'} - 1 \right] + E_0 \tag{4.6}$$

As mentioned previously, a second equation of state is necessary to ensure that the fit parameters are appropriate. The Birch-Murnaghan equation of state is chosen for this purpose [81]:

$$E(V) = E_0 + \frac{9V_0 B_0}{16}\left\{\left[\left(\frac{V_0}{V}\right)^{\frac{2}{3}} - 1\right]^3 B_0' + \left[\left(\frac{V_0}{V}\right)^{\frac{2}{3}} - 1\right]^2 \left[6 - 4\left(\frac{V_0}{V}\right)^{\frac{2}{3}}\right]\right\} \tag{4.7}$$

At absolute zero and low pressures, the parameters derived from the Murnaghan and Birch-Murnaghan fits should be equivalent.

Once the bulk modulus and its pressure derivative have been found, the shear elastic constants, y and y', are next computed. To determine the shear elastic constants, the method of Baskes is used [36]. In this method, the energy, E_0, of the reference structure, periodic in all three dimensions, is calculated. Next, a specific strain is applied to the same lattice, as given in Equation 4.8 [36]:

$$\begin{aligned} x' &= x + \varepsilon y, \quad & y' &= y, & z' &= z \quad \text{for } \gamma \\ x' &= (1+\varepsilon)x, \quad & y' &= \frac{y}{(1+\varepsilon)}, & z' &= z \quad \text{for } \gamma' \end{aligned} \tag{4.8}$$

where x,y,z are the reference lattice vectors, x',y',z' are the strained lattice vectors and ε is the strain coefficient. The atoms in the lattice are then relaxed while the periodic vectors are fixed at the strained values to yield the relaxed energy, E_1. Finally, Equation 4.9 is used to compute the shear elastic constants for cubic structures [38]:

$$\gamma, \gamma' = \frac{1}{\Omega}\frac{\partial^2 E}{\partial \varepsilon^2} \tag{4.9}$$

where Ω is the volume of the system which is conserved under each set of strained coordinates, as shown in Figure 4.1, and the second derivative of energy with respect to strain is given by [36]:

$$\left(\frac{\partial^2 E}{\partial \varepsilon^2}\right)_{\gamma} = \frac{2\left(E_1 - E_0\right)}{\varepsilon^2} \tag{4.10}$$

$$\left(\frac{\partial^2 E}{\partial \varepsilon^2}\right)_{\gamma'} = \frac{\left(E_1 - E_0\right)}{2\varepsilon^2} \tag{4.11}$$

for γ and γ' respectively. Combining Equations 4.9 and 4.10 and 4.9 and 4.11 gives linear expressions for energy versus ε^2, the slope of which is γ (4.12) and γ' (4.13):

$$\frac{2}{\Omega}\left(E_1 - E_0\right) = \varepsilon^2 \gamma \tag{4.12}$$

$$\frac{1}{2\Omega}\left(E_1 - E_0\right) = \varepsilon^2 \gamma' \tag{4.13}$$

The linear expressions for γ and γ' given by Equations 4.12 and 4.13 are valid only in the linear viscoelastic regime; that is, they hold for small values of ε only. In this work, energy is computed for ε from 0.5% to 1.0%, values which are large enough to avoid significant computational errors, but small enough to remain in the linear region.

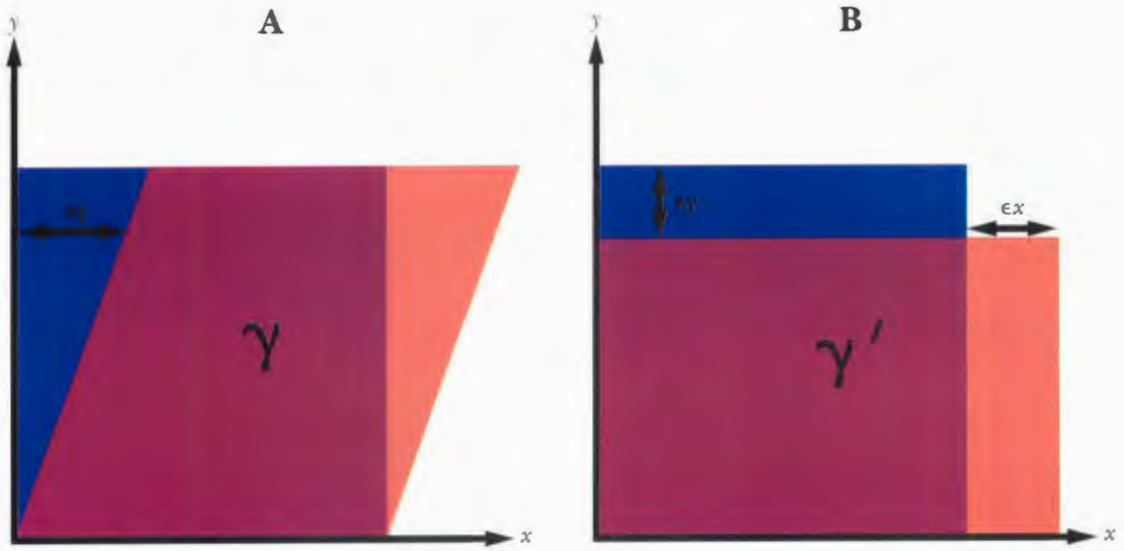

Figure 4.1: Schematic cross-section of the volume conserving strains γ (A) and γ' (B). In each figure, the blue region is representative of the unstrained lattice, while the red region is representative of the strained lattice.

The shear elastic constants, γ and γ', are related to the elastic constants, C_{11}, C_{12} and C_{44} by [36]:

$$\gamma = C_{44} \tag{4.14}$$

$$\gamma' = \frac{C_{11} - C_{12}}{2} \tag{4.15}$$

To separate C_{11} and C_{12} in Equation 4.15, an additional equation relating B, C_{11} and C_{12} is required [82]:

$$B = \frac{1}{3}(C_{11} + 2C_{12}) \tag{4.16}$$

Combining Equations 4.15 and 4.16, and solving for C_{11} and C_{12} gives:

$$C_{11} = B + \frac{4}{3}\gamma' \tag{4.17}$$

$$C_{12} = B - \frac{2}{3}\gamma' \tag{4.18}$$

Here, C_{11}, C_{12} and C_{44} form the complete elastic constant tensor for a cubic crystal system, which due to symmetry has only three independent parameters [82]:

$$C_{\eta} = \begin{pmatrix} C_{11} & C_{12} & C_{12} & \cdot & \cdot & \cdot \\ C_{12} & C_{11} & C_{12} & \cdot & \cdot & \cdot \\ C_{12} & C_{12} & C_{11} & \cdot & \cdot & \cdot \\ \cdot & \cdot & \cdot & C_{44} & \cdot & \cdot \\ \cdot & \cdot & \cdot & \cdot & C_{44} & \cdot \\ \cdot & \cdot & \cdot & \cdot & \cdot & C_{44} \end{pmatrix} \tag{4.19}$$

where, for readability, the dots represent zero. Additionally, the inverse of this matrix, S_{η}, will be required in the subsequent analysis:

$$S_{\eta} = C_{\eta}^{-1} = \begin{pmatrix} \frac{(C_{11}+C_{12})}{D} & \frac{C_{12}}{D} & -\frac{C_{12}}{D} & \cdot & \cdot & \cdot \\ -\frac{C_{12}}{D} & \frac{(C_{11}+C_{12})}{D} & -\frac{C_{12}}{D} & \cdot & \cdot & \cdot \\ -\frac{C_{12}}{D} & \frac{C_{12}}{D} & \frac{(C_{11}+C_{12})}{D} & \cdot & \cdot & \cdot \\ \cdot & \cdot & \cdot & \frac{1}{C_{44}} & \cdot & \cdot \\ \cdot & \cdot & \cdot & \cdot & \frac{1}{C_{44}} & \cdot \\ \cdot & \cdot & \cdot & \cdot & \cdot & \frac{1}{C_{44}} \end{pmatrix} \tag{4.20}$$

with

$$D = C_{11}^2 + C_{11}C_{12} - 2C_{12}^2 \tag{4.21}$$

Once B, C_{ij} and S_{ij} have been determined, an extensive thermoelastic analysis as performed by Mayer is carried out [83]. The benefits of this analysis are two-fold. First, additional parameters necessary to calculate curvatures and forces in cantilever systems, such as the shear modulus, Young's modulus and Poisson's ratio can be computed directly. In present work, these parameters are assumed equivalent to those of the substrate; this analysis provides an additional means to determine the parameters in the event that the additional layers are comparable in thickness to the substrate. Second, these calculations provide insight into the parameter B_0' (Equation 4.2). This parameter is difficult to measure experimentally (cf. Tables 5.5 and 5.6); in most work, the value used to fit B_0' is obtained directly from *ab initio* calculations. In what follows, it will be shown that B_0' can be related to two known physical quantities, the Grüneisen coefficient and the linear thermal expansion coefficient, and that present estimates of B_0' from *ab initio* calculations may be flawed.

To begin the additional thermoelastic analysis, the shear modulus, G, is computed using [83]:

$$G = G_{\text{Hill}} = \frac{1}{2}\left(G_{\text{Voigt}} + G_{\text{Reuss}}\right) \tag{4.22}$$

with:

$$5G_{\text{Voigt}} = C_{11} - C_{12} + 3C_{44} \quad \text{and}$$

$$\frac{5}{G_{\text{Reuss}}} = 4\left(S_{11} - S_{12}\right) + 3S_{11}$$

Knowledge of the shear and bulk moduli allows direct calculation of Poisson's ratio, ν, and the Young's modulus, Y, respectively [83]:

$$\nu = \frac{1}{2}\frac{B - \frac{2}{3}G}{B + \frac{1}{3}G} \tag{4.23}$$

$$Y = \frac{9B}{1 + 3\frac{B}{G}} \tag{4.24}$$

The shear and bulk moduli may also be used to compute the mean sound velocity, v_m [83]:

$$v_m = \left[\frac{1}{3}\left(\frac{2}{v_t^3} + \frac{1}{v_l^3}\right)\right]^{\frac{1}{3}} \tag{4.25}$$

where:

$v_t = \sqrt{\frac{G}{\rho}}$ is the transverse sound velocity,

$v_l = \sqrt{\frac{B + \frac{4}{3}G}{\rho}}$ is the longitudinal sound velocity, and

ρ is the density of the material.

which in turn is used to calculate the Debye temperature, T_D [83]:

$$T_D = \frac{h}{k_B}\left(\frac{6\pi^2 N}{V_0}\right)^{\frac{1}{3}} v_m \tag{4.26}$$

where N is the number of atoms in the unit cell and $\hbar$ and k_B are the reduced Planck and Boltzmann constants, respectively. Next, the Debye temperature is used to find the specific heat capacity, c_v [83]:

$$c_V(T) = 9Nk_B\left(\frac{T}{T_D}\right)^3 \int_0^{T_D/T} \frac{x^4 e^x}{\left(e^x - 1\right)^2} dx \tag{4.27}$$

Finally, the coefficient of linear thermal expansion, α_L, may be determined [83]:

$$\alpha_L(T) = \frac{1}{3}\gamma_G \frac{c_V(T)}{BV_0} \tag{4.28}$$

where γ_G is the Grüneisen coefficient, found by fitting energy as a function of volume to the following equation of state [83, 84]:

$$E(V) = \frac{BV_0}{\frac{5}{6} - \gamma_G}\left(\frac{V}{V_0}\right)^{\frac{5}{6}-\gamma_G}\left[\ln\left(\frac{V}{V_0}\right) - \frac{1}{\frac{5}{6} - \gamma_G}\right] + C \tag{4.29}$$

and $C = E_c$ is treated as a constant during the fit. Since the coefficient of linear thermal expansion is experimentally well-defined, this method provides an additional way to validate the Murnaghan / Birch-Murnaghan fits. Specifically, this formalism allows B_0' to be estimated indirectly using experimental data as will be discussed in Chapter 5.

4.2 Structural Energy Differences

The next series of data used to quantify the MEAM potential parameterization are the structural energy differences between the reference structure and the diamond, face centered cubic (FCC), body centered cubic (BCC), simple cubic (SC) and hexagonal close packed (HCP) structures. As in Section 4.1, the lattice constant for each structure is defined by the volume at which the energy is minimized.

Additionally, the energy difference, ΔE_α, between the reference structure and any other structure α is given by:

$$\Delta E_\alpha = E_\alpha - \frac{N_\alpha}{N_{\text{ref}}} E_{\text{ref}} \tag{4.30}$$

where E_α and E_{ref} are the minimized energies and N_α and N_{ref} are the number of atoms for the α structure and the reference structure, respectively. A summary of the primitive and basis vectors for each structure used in this work is given in Table 4.1.

4.3 Point Defects

Point defects in the form of vacancies and interstitials are next considered[1]. In each case, a reference supercell consisting of 10×10×10 primitive cells is constructed. Periodic boundary conditions are not employed[2]; rather, the outer five layers along each direction $\pm x$, $\pm y$ and $\pm z$ are fixed and removed from the energy calculations to simulate bulk conditions within the cell as shown schematically in Figure 4.2. The first step in either defect calculation is to compute the energy, E_0, of the reference cell. After computing E_0, the atom at (0,0,0) is removed to create a vacancy, and the

[1]Point defects are chosen due to the availability of experimental data. Further, interfacial mixing (refer to Chapter 1) will create disruptions in the periodicity of the bulk lattice(s) which are observed in the form of vacancies and interstitials.

[2]The choice of (non)periodic boundary conditions and supercell size are not critical. Negligible differences in energy are observed provided the supercell is large enough to prevent replication of the defect in the case of the periodic regime, and to spatially allow enough unfrozen atoms to permit complete relaxation of the atoms surrounding the defect (typically, this includes the third to fourth nearest neighbours). This particular method was adopted since nonperiodic simulations are computationally more efficient than their periodic counterparts, and a 10×10×10 supercell always allows sufficient free atoms for complete relaxation.

resultant system is relaxed with energy E_1. The relaxed vacancy formation energy, E_v^f, is thus:

$$E_v^f = E_1 - \frac{N-1}{N} E_0 \tag{4.31}$$

where N is the number of atoms in the reference supercell. The vacancy migration energy, E_v^{mig}, is defined to be the difference between the total energy of the system before the migration of an atom, E_1, and the saddle point energy, E_{SP}, during migration:

$$E_v^{mig} = E_{SP} - E_1 \tag{4.32}$$

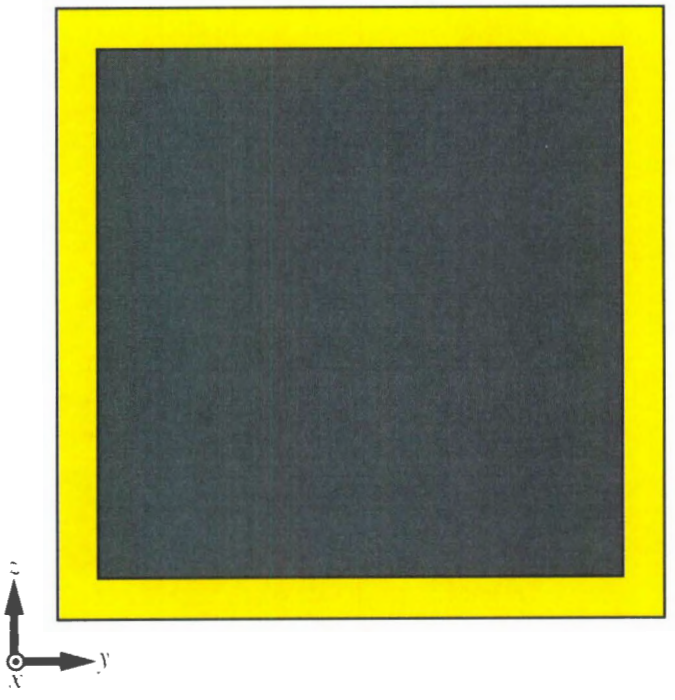

Figure 4.2: Schematic representation of the 2D cross-section of the supercell constructed for point defect calculations. Here, the yellow areas represent layers of atoms which are frozen and removed from the energy computation, while the grey area represents atoms which are free to move about the cell.

Table 4.1: Summary of the primitive and basis vectors for the structures considered in structural energy difference calculations.

Structure	Primitive Vectors	No. Basis Atoms	Basis Vectors
Simple Cubic (SC)	$A_1 = a(1,0,0)$ $A_2 = a(0,1,0)$ $A_3 = a(0,0,1)$	1	$B_1 = (0,0,0)$
Face Centered Cubic (FCC)	$A_1 = \frac{a}{2}(0,1,1)$ $A_2 = \frac{a}{2}(1,0,1)$ $A_3 = \frac{a}{2}(1,1,0)$	1	$B_1 = (0,0,0)$
Body Centered Cubic (BCC)	$A_1 = \frac{a}{2}(-1,1,1)$ $A_2 = \frac{a}{2}(1,-1,1)$ $A_3 = \frac{a}{2}(1,1,-1)$	1	$B_1 = (0,0,0)$
Diamond Cubic	$A_1 = \frac{a}{2}(0,1,1)$ $A_2 = \frac{a}{2}(1,0,1)$ $A_3 = \frac{a}{2}(1,1,0)$	2	$B_1 = \frac{1}{8}(1,-1,-1)$ $B_2 = \frac{1}{8}(1,1,1)$
Hexagonal Close Packed (HCP)	$A_1 = \frac{a}{2}(1, \sqrt{3},0)$ $A_2 = \frac{a}{2}(1,\sqrt{3},0)$ $A_3 = c(0,0,1)$	2	$B_1 = \left(\frac{1}{3},\frac{2}{3},\frac{1}{4}\right)$ $B_2 = \left(\frac{2}{3},\frac{1}{3},\frac{3}{4}\right)$

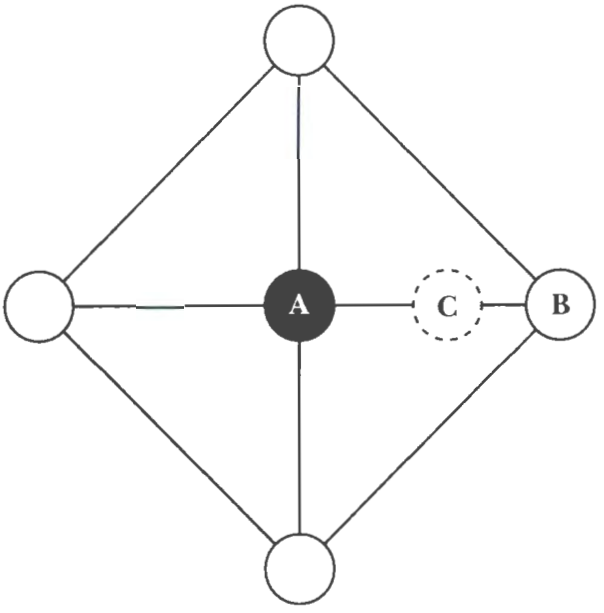

Figure 4.3: Schematic representation of the method to compute the vacancy migration energy. In this figure, position A represents a vacancy, position B represents a nearest neighbour atom and position C represents the maximum energy (saddle point) along the linear path B to A.

where the saddle point energy is computed as follows [85]. First, in reference to Figure 4.3, it is assumed that the migration of a vacancy from position **A** to **B** is energetically equivalent to the migration of an atom from position **B** to **A**. At the saddle point, corresponding to position **C**, the energy of the system is at a maximum for this particular migration route. The atom is fixed at position **C**, and the other atoms are allowed to fully relax. This energy corresponds to the saddle point energy.

Finally, the activation energy of vacancy diffusion, Q, is merely the sum of the formation and migration energies:

$$Q \quad E_v^f + E_v^{\mathrm{mig}} \tag{4.33}$$

To compute the energy of the interstitials, rather than remove the atom at (0,0,0), an additional atom is inserted at a specific coordinate as described in Table 4.2. As in the vacancy calculations, the lattice with the interstitial is relaxed, yielding energy E_1. The relaxed interstitial formation energy, E_f^I, is then:

$$E_f^I = E_1 - \frac{N+1}{N} E_0 \tag{4.34}$$

Table 4.2: Summary of the interstitial coordinates considered in this work.

HOST STRUCTURE	INTERSTITIAL NAME	INTERSTITIAL COORDINATE
Diamond Cubic	Tetrahedral[1]	$R_I^I \approx \left(\frac{1}{4},\frac{1}{4},\frac{3}{4}\right)$
Diamond Cubic	Hexagonal[1]	$R_I^{II} \approx \left(\frac{1}{8},\frac{1}{8},\frac{5}{8}\right)$
Face Centered Cubic	[100] Dumbbell[2]	Figure 4.4

[1] Reference [86]
[2] Reference [87]

4.4 SURFACE PROPERTIES

To compute the surface properties of the system, a 10×10×10 supercell is again constructed. For this application, the bottom five layers along -z are frozen and omitted from the energy calculation to simulate the bulk material, as shown in Figure 4.5. The system is periodic in x and y but not z; the top layer along +z is the free surface layer to be studied. The surface configurations considered in this work are summarized in Table 4.3.

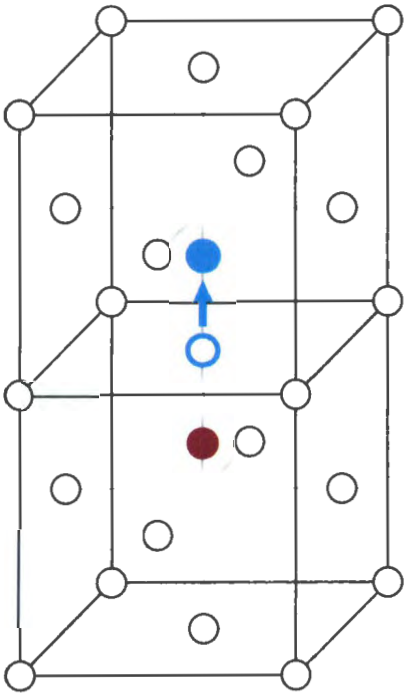

Figure 4.4: The FCC [100] Dumbbell interstitial. The solid blue circle depicts an atom shifted from its initial face centered position, while the solid red circle represents an inserted interstitial atom.

In each configuration α, the energy per surface atom, E_α^{atom}, is given by:

$$E_\alpha^{\text{atom}} = E_\alpha^{\text{bulk}} - \frac{N_\alpha^{\text{bulk}}}{N_{\text{ref}}} E_{\text{ref}} \tag{4.35}$$

where E_α^{bulk} and E_{ref} are the energies and N_α^{bulk} and N_{ref} are the number of atoms in the α and reference supercells respectively. It is also beneficial to consider the surface energy as a per area quantity, E_α^{area}, as doing so permits direct comparison with experimental data:

$$E_\alpha^{\text{area}} = \frac{N_\alpha^{\text{bulk}}}{A_\alpha} E_\alpha^{\text{atom}} \tag{4.36}$$

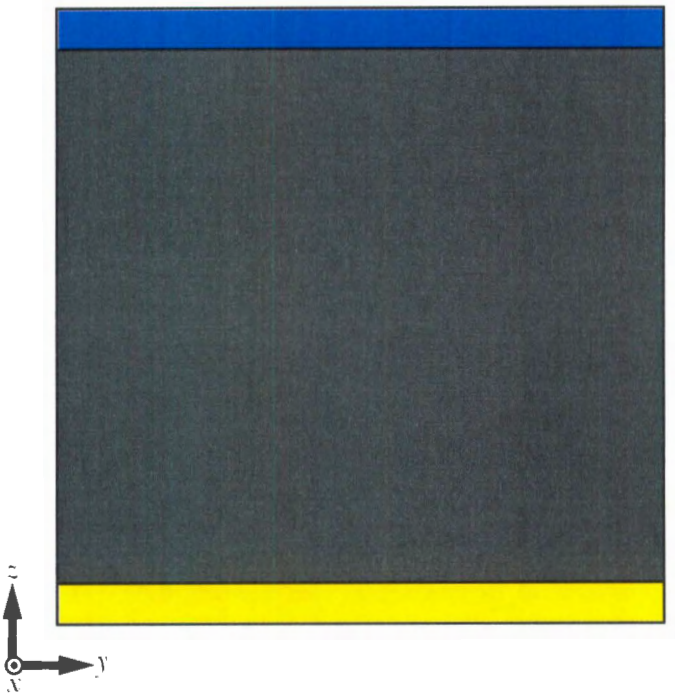

Figure 4.5: Schematic representation of the 2D cross-section of the supercell constructed for surface energy calculations. Here, the yellow area represents layers of atoms which are frozen and removed from the energy computation, the grey area represents atoms which are free to move about the cell, and the blue area represents the free surface to be studied.

where A_α is the surface area of the supercell in configuration α. Finally, the relative plane spacing, Δd_α^{12}, is defined as:

$$\Delta d_\alpha^{12} = \frac{d_\alpha^{12}}{d_{\text{ref}}^{12}} \tag{4.37}$$

where d_α^{12} and d_{ref}^{12} are the distances between the surface plane and its nearest neighbour in the α and reference supercells respectively.

Table 4.3: Summary of the surface configurations considered in this work.

Host Structure	Surface Plane	Config.	Description
Diamond Cubic Face Centered Cubic	(100) (110) (111)	Ideal	Atoms in reference configuration; Energy computed without relaxation
Diamond Cubic Face Centered Cubic	(100) (110) (111)	1×1 Relaxed	Atoms in reference configuration; Energy minimized thereby relaxing surface atoms along z
Diamond Cubic	(100)	2×1 Dimer	Atoms in 2×1 configuration (Figure 4.6A); Energy minimized thereby relaxing surface atoms along z
Face Centered Cubic	(100)	1×5 Hexagonal	Atoms in 1×5 configuration (Figure 4.6B); Energy minimized thereby relaxing surface atoms along z
Face Centered Cubic	(110)	1×2 Missing Row	Atoms in 1×2 configuration (Figure 4.6C); Energy minimized thereby relaxing surface atoms along z

4.5 Alloys

The alloy (SiAg, SiAu and AgAu) parameters are determined using the properties of binary clusters, which are available experimentally, and structural energy differences, which are calculated using DFT. An exhaustive literature survey indicates that SiAg, SiAu and AgAu do not form stable alloys, and so the extensive experimental data used to fit the elements is not available for the alloys. Fortunately, there are fewer parameters to consider in the alloy fits (n_i^0, E_{ij}^0, α_{ij}, $\mathbf{R}_{ij}^0$ $\mathbf{att}_{ij}$, $\mathbf{rep}_{ij}$, $C_{\min}(i,j,k)$ and $C_{\max}(i,j,k)$); the limited properties used here are sufficient to determine them.

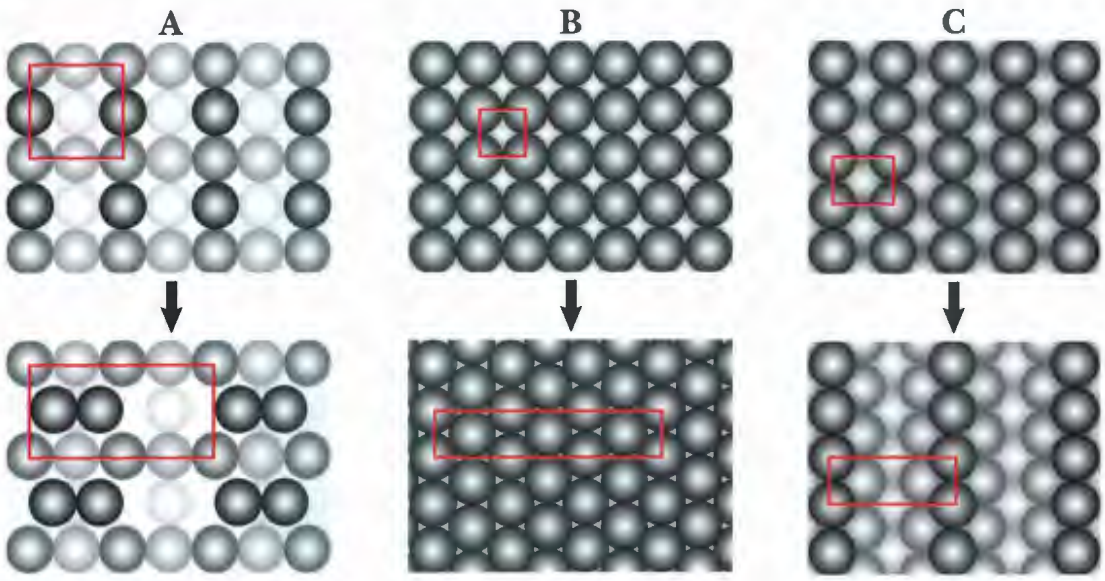

Figure 4.6: Diamond cubic (100)2x1 reconstruction (A), FCC (100)1x5 reconstruction (B), and FCC (110)1x2 reconstruction (C). In each figure, the top image represents the ideal configuration, while the bottom image depicts the reconfigured surface. Additionally, darker shaded atoms are closer to the surface than lighter ones.

For the binary clusters, the binding energy per atom, E_B, and the equilibrium bond length, $\mathbf{R}^{\text{clust}}$, are considered. To begin, energy is minimized by adjusting the bond length, and the length which corresponds to the energy minimum is $\mathbf{R}^{\text{clust}}$. E_B is then simply:

$$E_B = \frac{1}{2}\left(E_{\text{sys}} - E_i - E_j\right) \tag{4.38}$$

where E_{sys} is the minimized total energy of the binary system and E_i and E_j are the energies of the constituent atoms in the cluster.

For the structural energy differences, a variety of standard binary and ternary crystallographic structures are utilized, as summarized in Table 4.4. Computational details are exactly as described in Section 4.1.

Table 4.4: Summary of the primitive and basis vectors for the structures considered in structural energy difference calculations.

Struct.	Primitive Vectors	No. Basis Atoms	Basis Vectors
B1 (NaCl) SiAg SiAu AgAu	$A_1 = \frac{a}{2}(0,1,1)$ $A_2 = \frac{a}{2}(1,0,1)$ $A_3 = \frac{a}{2}(1,1,0)$	2	$B_1 = (0,0,0)$ (Na) $B_2 = \frac{1}{2}(1,1,1)$ (Cl)
$L1_2$ (Cu_3Au) Si_3Ag Ag_3Si Si_3Au Au_3Si Au_3Ag Ag_3Au	$A_1 = a(1,0,0)$ $A_2 = a(0,1,0)$ $A_3 = a(0,0,1)$	4	$B_1 = (0,0,0)$ (Au) $B_2 = \frac{1}{2}(0,1,1)$ (Cu) $B_3 = \frac{1}{2}(1,0,1)$ (Cu) $B_4 = \frac{1}{2}(1,1,0)$ (Cu)
$E2_1$ ($CaTiO_3$) $AgAuSi_3$	$A_1 = a(1,0,0)$ $A_2 = a(0,1,0)$ $A_3 = a(0,0,1)$	5	$B_1 = (0,0,0)$ (Ca) $B_2 = \frac{1}{2}(1,1,1)$ (Ti) $B_3 = \frac{1}{2}(0,1,1)$ (O) $B_4 = \frac{1}{2}(1,0,1)$ (O) $B_5 = \frac{1}{2}(1,1,0)$ (O)

Struct.	Primitive Vectors	No. Basis Atoms	Basis Vectors
Diamond Subst. (A_2B) Si_2Ag Si_2Au	$A_1 = a(1,0,0)$ $A_2 = a(0,1,0)$ $A_3 = a(0,0,1)$	8	$B_1 = (0,0,0)$ (B) $B_2 = \frac{1}{2}(0,1,1)$ (A) $B_3 = \frac{1}{2}(1,0,1)$ (A) $B_4 = \frac{1}{2}(1,1,0)$ (A) $B_5 = \frac{1}{4}(1,1,1)$ (A) $B_6 = \frac{1}{4}(3,3,1)$ (A) $B_7 = \frac{1}{4}(3,1,3)$ (A) $B_8 = \frac{1}{4}(1,3,3)$ (A)
c116 ($CrFe_4Ni_3$) $AuSi_4Ag_3$	$A_1 = \frac{a}{2}(-1,1,1)$ $A_2 = \frac{a}{2}(1,-1,1)$ $A_3 = \frac{a}{2}(1,1,-1)$	8	$B_1 = (0,0,0)$ (Cr) $B_2 = \frac{1}{2}(1,1,1)$ (Fe) $B_3 = \frac{1}{2}(1,0,0)$ (Fe) $B_4 = \frac{1}{2}(0,1,0)$ (Fe) $B_5 = \frac{1}{2}(0,0,1)$ (Fe) $B_6 = \frac{1}{2}(0,1,1)$ (Ni) $B_7 = \frac{1}{2}(1,0,1)$ (Ni) $B_8 = \frac{1}{2}(1,1,0)$ (Ni)

Struct.	Primitive Vectors	No. Basis Atoms	Basis Vectors	
$L2_1$ ($AlCu_2Mn$) $SiAu_2Ag$	$A_1 = \frac{a}{2}(0,1,1)$ $A_2 = \frac{a}{2}(1,0,1)$ $A_3 = \frac{a}{2}(1,1,0)$	4	$B_1 = (0,0,0)$ $B_2 = \frac{1}{2}(-1,1,1)$ $B_3 = \frac{1}{4}(-1,-1,-1)$ $B_4 = \frac{1}{4}(1,1,1)$	(Al) (Mn) (Cu) (Cu)

5. Results and Discussion

5.1 Computational Method

5.1.1 Density Functional Theory

DFT calculations[1] were performed using the ABINIT code version 5.8.3 [88, 89] within the GGA. The exchange-correlation functional used was that of Perdew, Burke and Ernzerhof[2] [55]. A Monkhorst-Pack 16×16×16 k-point grid was used in all computations [65]. The electronic wavefunctions were expanded in plane waves with a kinetic energy cut-off of 25 Hartree. In all computations, total energy was converged to approximately 0.1 meV with respect to k-point sampling, energy cut-off and cell size.

Pseudopotentials were generated using the OPIUM software version 3.1 [90] and the RRKJ optimized method [69] with a target kinetic energy cut-off of 25 Hartree.

[1]Single-threaded computations were executed on ACENet clusters Placentia2, Mahone2 and Glooscap. Simulation times vary on the order of one week (elements) to one month (ternary alloys).

[2]In order to remain norm-conserving, the pseudopotential is correlated to all-electron results computed with a given exchange-correlation functional. For this reason, it is critical that the pseudopotential generator and the DFT package employ the same XC functional. At present, OPIUM, FHIPP and others cannot create pseudopotentials using advanced XC functionals, and so the PBE GGA functional common to both OPIUM and ABINIT was chosen.

Scalar relativistic corrections were included in the pseudopotentials for Ag and Au; no relativistic corrections were necessary for Si. Valence and core orbitals, orbital occupations, optimization radii and eigenvalue estimates were chosen such that transferability was maximized (<135 meV error per configuration in Table 5.1), discrepancies between all-electron and pseudopotential calculations were minimized (<2 meV) and the resultant pseudopotential properly reproduced experimental results (equilibrium bond length, cohesive energy, bulk modulus and vacancy formation energy). A summary of the electronic configurations chosen for Ag, Au and Si is presented in Table 5.1.

Table 5.1: Electronic configurations used in the generation of pseudopotentials. Here, the reference electron configuration is provided for the elements, as well as the electronic orbitals deemed to be valence or core electrons along with their occupations for the pseudopotentials. Finally, the valence configurations tested for transferability are provided.

Elt.	# of e⁻ ref/pp	Ref. e⁻ Config.	PP Core	PP Valence	Transf. Config.
Si	14 14	$1s^2$	$1s^2$	$3s^2p^2d^0$	$3s^1p^2d^0$
		$2s^2p^6$	$2s^2p^6$		$3s^2p^1d^0$
		$3s^2p^2$			$3s^2p^2d^0$
Ag	47 46	$1s^2$	$1s^2$	$4d^{10}$	$4d^95s^0p^0$
		$2s^2p^6$	$2s^2p^6$	$5s^0p^0$	$4d^{10}5s^1p^0$
		$3s^2p^6d^{10}$	$3s^2p^6d^{10}$		$4d^{10}5s^0p^1$
		$4s^2p^6d^{10}$	$4s^2p^6$		$4d^{10}5s^1p^1$
		$5s^1$			
Au	79 78	$1s^2$	$1s^2$	$5d^0$	$5d^96s^0p^0$
		$2s^2p^6$	$2s^2p^6$	$6s^1p^0$	$5d^{10}6s^0p^0$
		$3s^2p^6d^{10}$	$3s^2p^6d^{10}$		$5d^{10}6s^1p^0$
		$4s^2p^6d^{10}f^{14}$	$4s^2p^6d^{10}f^{14}$		$5d^{10}6s^0p^1$
		$5s^2p^6d^{10}$	$5s^2p^6$		$5d^{10}6s^1p^1$
		$6s^1$			

5.1.2 Modified Embedded Atom Method

MEAM computations[3] were completed using the Large-scale Atomic/Molecular Massively Parallel Simulator (LAMMPS) software package versions 21-May-08 (elements) and 7-Jul-09 (elements/alloys) [91]. The automated parameter fitting procedure is as follows. An initial data set of 1,500 entries, an example of which is provided in Figure 5.1, is collected with the MEAM parameters assigned randomly over an extreme range, as shown in Table 5.2. The minimum parameter resolution (step-size) is 0.1. The bulk modulus and elastic constants, identified as the critical parameters in the MEAM fit [36 – 38], are used to decide whether or not to compute a full data set. For the initial step, a ±20% tolerance is used: should the computed result differ with the experimental value by more than this, the computation is stopped and the parameter set discarded.

Table 5.2: Initial parameter ranges for MEAM fit algorithm.

Parameter	Minimum	Maximum
α_i	0.1	10.0
A_i	0.1	5.0
$\beta_i^{(0)}$	-10.0	10.0
$t_i^{(0)}$	-10.0	10.0
att/rep	0.0	10.0
C_{min}	0.5	3.0
C_{max}	$>C_{min}$	6.0

[3]Multi-threaded (MPICH2) computations were executed on ACENet clusters Placentia2, Mahone2 and Glooscap and a local sever (Baskes). For the fit procedure, deployment across four cores was optimal with the system sizes considered. On Baskes, elastic constant calculations execute on the order of thirty seconds; a complete data set takes on the order of five to eight minutes to compute.

```
# ------------------------------------------------------------------------
# STEP 1:                                                          1/1500
# ------------------------------------------------------------------------
# alpha,asub,t1,t2,t3,b0,b1,b2,b3,cmax,cmin,delr,rc,att,rep
# 6.05,1.082,4.319,2.331,3.049,4.41,3.701,6.248,2.588,2.5,1.58,0.0,0.0
@ ------------------------------------------------------------------------
     LC              4.0871  4.09
     EN              2.85    2.85
     mBM             0.6772  0.678443
     gBM             0.6786  0.678443
     BMD             4.9576  ?
     gGAM            2.341   ?
     G               0.3187  0.318936
     GP              0.1067  ?
     G/GP            2.9881  ?
     C11             0.8194  0.82075
     C12             0.6061  0.60729
     rBCC            3.2152  3.282
     rHCP            4.1832  ?
     rSC             2.6607  2.812
     rDIA            6.0242  6.402
     eBCC            0.0465  0.04
     eHCP            2.1436  0.003
     eSC             0.1361  0.31
     eDIA            0.5576  0.66
     vFE             1.165   1.1
     vfDE            1.6317  1.77
     vME             0.4667  0.67
     E-100-ID        0.6431  ?
     E-100-1x1       0.6161  ~0.7
     D-100-1x1       2.1501  2.006
     E-100-HEX       72.0125 GT_1x1
     D-100-HEX       2.045   ?
     E-110-ID        0.7995  ?
     E-110-1x1       0.7758  ~0.7
     D-110-1x1       1.3947  2.574-2.690
     E-110-1x2       0.9524  GT_1x1
     D-110-1x2       1.2878  ?
     E-111-ID        4.1864  ?
     E-111-1x1       0.7973  ~0.7
     D-111-1x1       2.399   2.314-2.361
     (100)DB         2.7559  2.86
! ------------------------------------------------------------------------
```

Figure 5.1: Sample MEAM data entry.

Once the initial 1,500 entries have been computed, the data is next analysed. The mean-absolute error (MAE) is computed for each entry:

$$\mathrm{MAE} = \frac{1}{N}\sum_{i=1}^{N}\left|f_i^{\mathrm{calc}} - f_i^{\mathrm{expt}}\right| \tag{5.1}$$

where f_i^{calc} is the calculated MEAM value, f_i^{expt} is the experimental value and N is the number of values per entry. The entries are sorted by MAE, and the ten entries with the lowest MAE are considered. New ranges are defined for each MEAM parameter by simply considering the minimum and maximum values +5% of a particular parameter in the truncated data set. An additional 500 entry data set is collected with the redefined parameter ranges, a parameter step-size of 0.05 and a tolerance of 5% on the bulk modulus and elastic constants. The parameter ranges, step-sizes and tolerances are continually refined until the desired parameterization is found. The final, refined parameter sets are as summarized in Table 5.3. In the subsequent sections, the parameters identified in Chapter 4 will be examined.

5.2 Elements

To begin, the static structural properties, including the lattice constant, cohesive energy, equilibrium volume and bulk modulus were determined for each element by considering the energy vs. volume data. The results are summarized in Figures 5.2 through 5.4 for Si, Ag and Au respectively. Due to the inherent difficulties in constructing pseudopotentials which reproduce exactly the experimental results, two figures are provided for each element: the as-obtained data for the DFT and MEAM calculations, and an additional graph depicting the DFT and MEAM calculations

with a common origin to highlight the similarity in curvatures[1]. The agreement between the MEAM results and experimental data is exemplary, and the DFT computations provide the proper curvatures and are within 2.5% of the experimental values for cohesive energy and lattice constant.

Table 5.3: Final MEAM parameter set.

PARAM	Si	Ag	Au	SiAg	SiAu	AgAu	SiAgAu
E_i^0	4.63	2.85	3.93	3.37	4.27	2.60	
$\mathbf{R}_i^0$	2.35	2.89	2.88	2.68	2.54	2.48	
α_i	4.87	6.05	6.61	5.07	4.91	6.19	
n_i^0	5.35	2.25	1.76				
A_i	1.007	1.078	1.038				
$\beta_i^{(0)}$	4.003	4.414	5.436				
$\beta_i^{(1)}$	3.122	3.698	4.180				
$\beta_i^{(2)}$	7.422	6.244	4.900				
$\beta_i^{(3)}$	7.434	2.578	3.600				
$t_i^{(0)}$	1	1	1				
$t_i^{(1)}$	4.292	4.326	1.737				
$t_i^{(2)}$	5.118	2.335	1.950				
$t_i^{(3)}$	-1.193	3.049	2.729				
att	0	0	0	0.57	0.13	0.21	
rep	0	0	0	0.94	1.64	0.05	
$C_{\min}$	1.70	1.60	1.50	(Si,Si,Ag): 1.50 (Si,Ag,Ag): 1.68	(Si,Si,Au): 2.29 (Si,Au,Au): 1.50	(Ag,Ag,Au): 1.30 (Ag,Au,Au): 1.21	1.06
$C_{\max}$	4.00	2.52	3.26	(Si,Si,Ag): 3.50 (Si,Ag,Ag): 4.31	(Si,Si,Au): 2.48 (Si,Au,Au): 3.72	(Ag,Ag,Au): 4.20 (Ag,Au,Au): 4.91	4.54

[1]This is done for display purposes only; the *common origin* graphs have no bearing on the MEAM fits.

Next, the thermoelastic results for Si, Ag and Au are presented in Tables 5.4, 5.5 and 5.6 respectively. The results are, in general, excellent. For Si, the MAE (cf. Equation 5.1) in this work is 0.9, compared to the MAE of 2.7 for the first nearest neighbour parameterization of Baskes [36] and 2.6 for the second nearest neighbour parameterization of Lee [37]. Note that these MAEs were computed using only parameters common to all groups with a well-defined experimental value. Similarly, for Ag and Au, the MAE in this work are 0.3 and 0.2, compared to the second nearest neighbour parameterization of Baskes [38] which gave a MAE in each case of 0.1.

It is interesting to note the large disagreement with the coefficient of linear thermal expansion, α, for Si. As this parameter is a function of the bulk modulus, specific heat capacity, equilibrium volume and Grüneisen coefficient, the only truly unknown variable is the Grüneisen coefficient as the other parameters agree strongly with experimental values. Thus, one may solve Equation 1.28 for the Grüneisen coefficient, assuming that α takes the experimental value of 2.6×10^{-6} K^{-1}. The resultant Grüneisen coefficient is 0.93; slightly higher than the value presented in literature [93]. Using this value, one may construct a theoretical set of energy vs. volume data to which to complete a Murnaghan fit. The result, as depicted in Figure 5.5, suggests that the value of B_0' may necessarily be closer to 2.2 rather than the 4.2 suggested by *ab initio* calculations[5].

[5]The bulk modulus pressure derivative, B_0', and the Grüneisen coefficient, γ_G, are difficult to empirically correlate, as shown by Slater and others [95]. γ_G, which is a measure of the variation of pressure with internal energy at a constant volume, and B_0' both serve as a link between the elastic and thermal properties. In order to understand fully the implications of the adjusted B_0' value, one must consider higher order elastic constants, as well as high pressure thermal and elastic properties in conjunction with the low pressure values given in this work.

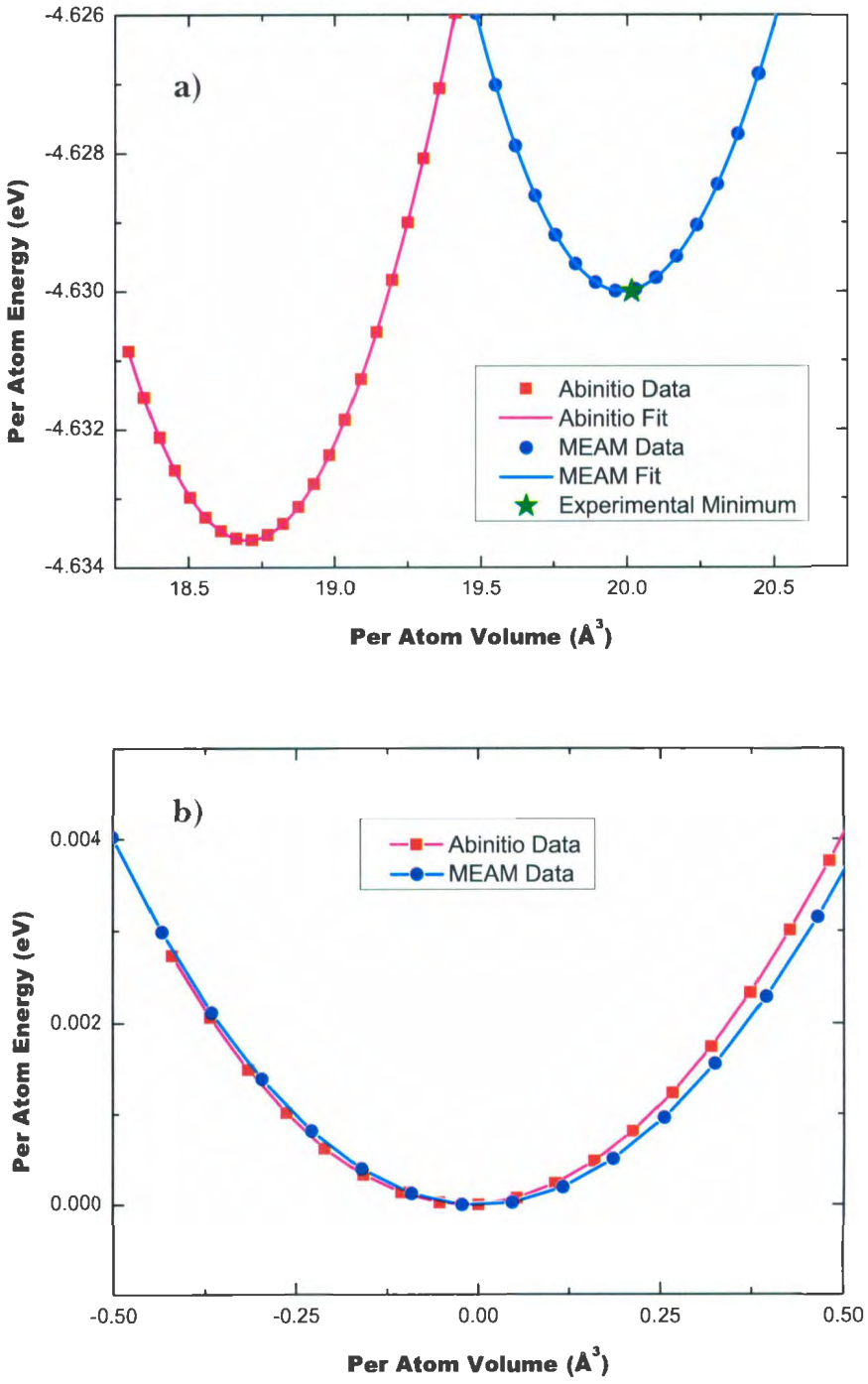

Figure 5.2: DFT and MEAM energy vs. volume curves for Si. a) Data as-obtained. b) Data recentered to common origin.

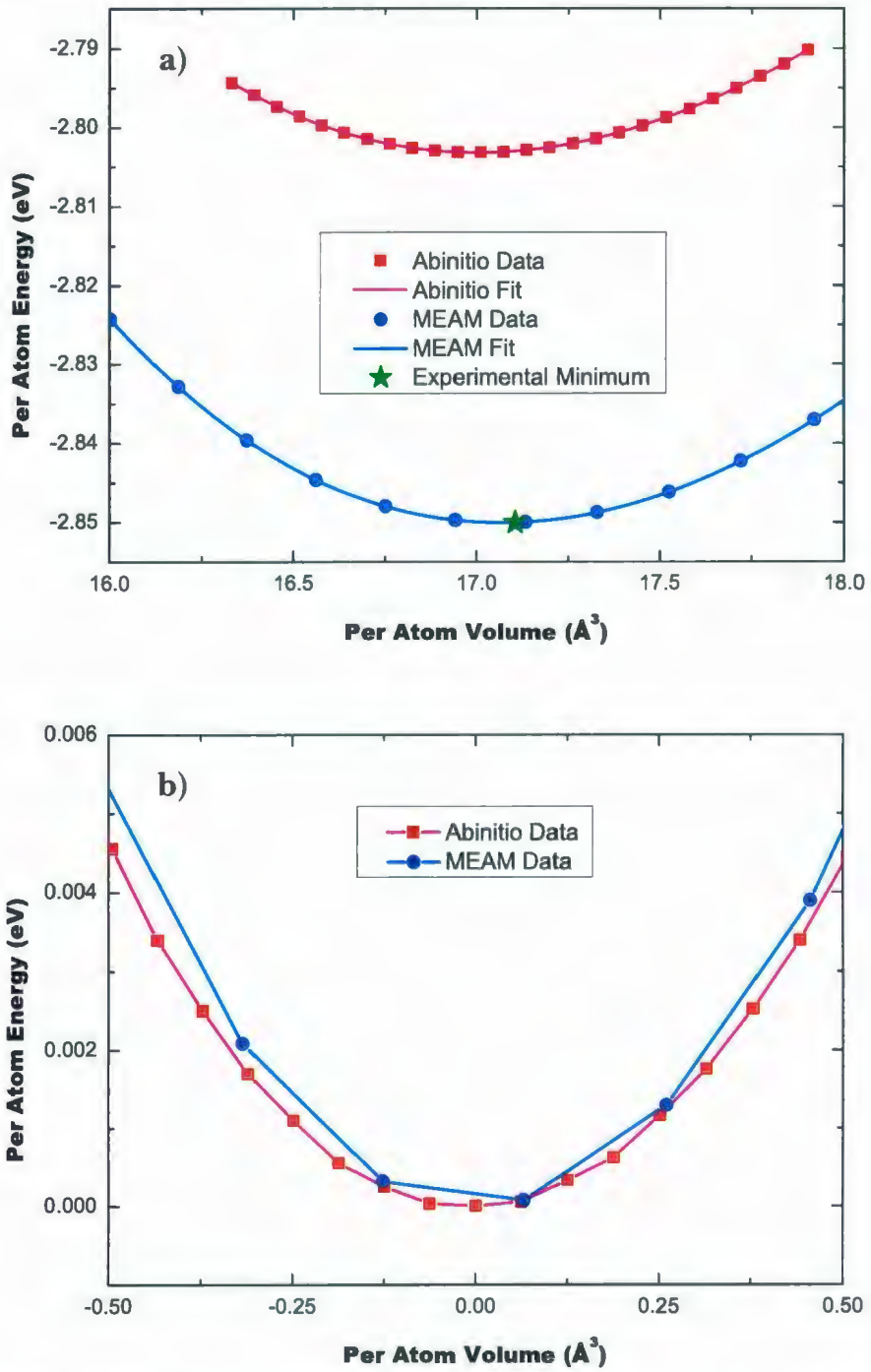

Figure 5.3: DFT and MEAM energy vs. volume curves for Ag. a) Data as-obtained. b) Data recentered to common origin.

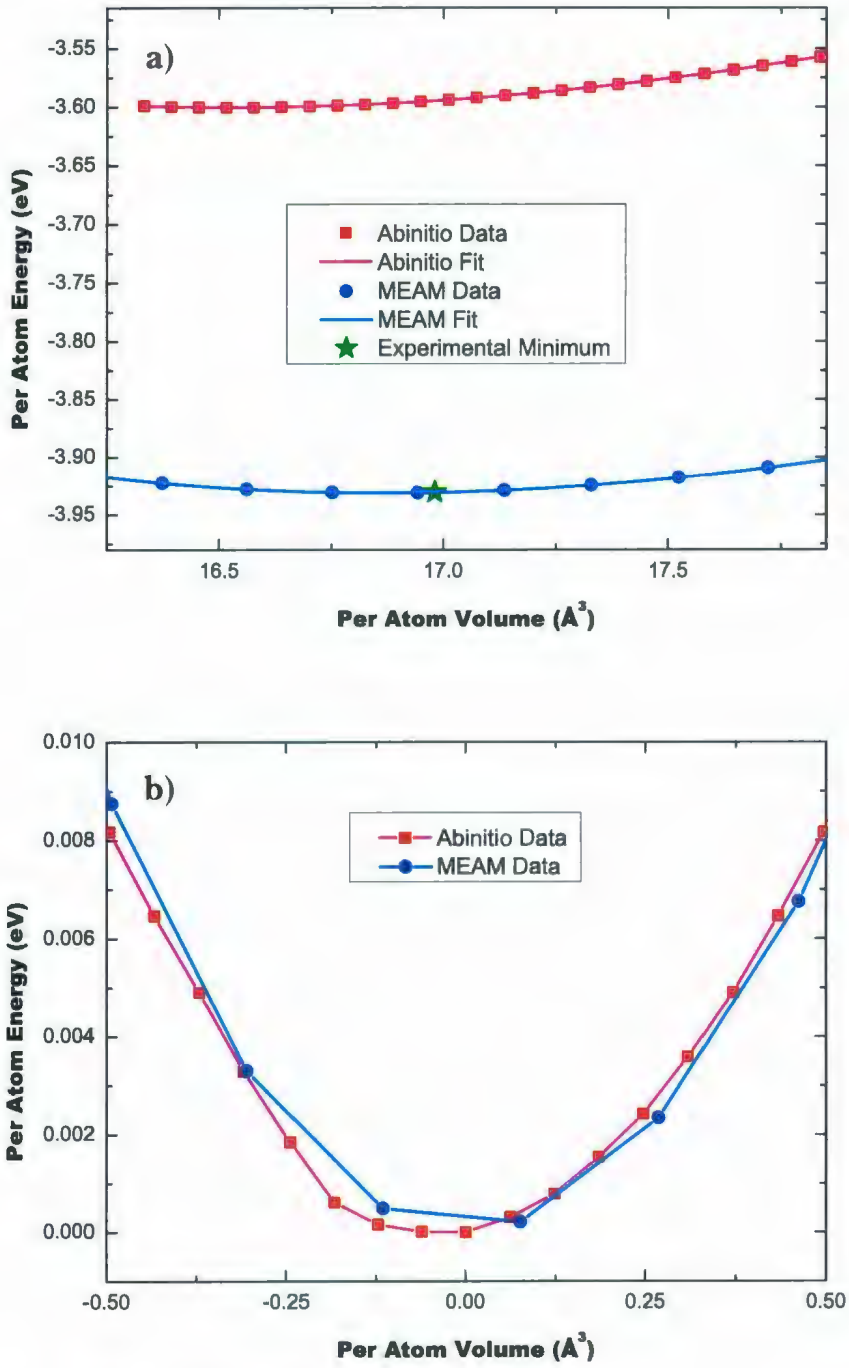

Figure 5.4: DFT and MEAM energy vs. volume curves for Au. a) Data as-obtained. b) Data recentered to common origin.

Table 5.4: Thermoelastic results for Si. Distances are given in Angströms, energies in eV, elastic properties in GPa, velocities in m/s, temperatures in K, heat capacities in J/mol·K, and thermal expansion coefficients in 10^{-6} K^{-1}. Thermal properties are computed at 293 K. Data from [37] unless otherwise noted.

For comparison with other empirical semiconductor potentials, values for the Stillinger-Weber (SW), Tersoff (Ters), Environment-Dependent Interatomic Potential (EDIP), Highly Optimized Empirical Potential (HOEP) and first (1NN) and second (2NN) nearest neighbour MEAM are provided from literature [37]. A schematic representation of this data is presented in Figure 5.6.

								This Work	
	Expt/					1NN	2NN		1NN
	DFT	SW	Ters	EDIP	HOEP	MEAM	MEAM	DFT	MEAM
a	5.431							5.31	5.431
E_c^0	-4.63							-4.63	-4.63
B_0	97.7[c] 99	108	98	99	110	98	99	96.2	99.0
B_0'	4.2	2.93	4.3				4.27	4.01	4.22
γ/C_{11}	79.3[c] 80	60	69	71	72	79	79		79
γ'	50.5					50			50.6
C_{11}	168	162	143	175		164	164		165
C_{12}	65	82	75	62		64	67		64
C_{11}-C_{12}	103	80	68	113	83	100	97		101
C_{11}-C_{44}	-15	22	6	-9		-15	-12		-15
G	52[c]								66.1
Y	185[c]								162
ν	0.28[c]								0.22
γ_G	0.25[c]							2.52	1.75
v_l									5325
v_t									8930
v_m	8433[d]								5894
T_D	646[d]								645
c_v	19.8[d]								19.8
α_l	2.6[d]								4.89

[c] Reference [36]
[d] Reference [92]
[e] Reference [93]

Table 5.5: Thermoelastic results for Ag. Distances are given in Angströms, energies in eV, elastic properties in GPa, velocities in m/s, temperatures in K, heat capacities in J/mol·K, and thermal expansion coefficients in 10^{-6} K^{-1}. Thermal properties are computed at 293 K. Data from [39] unless otherwise noted.

				This Work	
	Expt/ DFT	1NN MEAM[+]	2NN MEAM	DFT	1NN MEAM
a	4.09			4.08	4.09
E_c^0	2.85			2.80	2.85
B_0	108.7			98.1	108.5
B_0'	5.87 3.76 – 6.12[‡]		5.61	5.57	4.96
γ / C_{11}	51.1	46.5	51.1		51.1
γ'		16			17.1
C_{11}	131.5		131.5		131.3
C_{12}	97.3		97.3		97.1
C_{11}-C_{12}			34.2		34.2
C_{11}-C_{44}			46.2		46
G	30[†]				33
Y	83[†]				89.9
ν	0.37[†]				0.36
γ_G	2.4 2.2[‡] 2.35[#]			2.77	2.34
v_l					1772
v_t					3811
v_m	2680[†]				1996
T_D	225[†]				230
C_v	25.2[†]				24.2
α_l	19.1[†]				16.9

[+] Reference [38]
[‡] Reference [84]
[†] Reference [92]
[‡] Reference [93]
[#] Reference [94]
[†] Reference [95] (experimentally assessed values of B_0')

Table 5.6: Thermoelastic results for Au. Distances are given in Angströms, energies in eV, elastic properties in GPa, velocities in m/s, temperatures in K, heat capacities in J/mol·K, and thermal expansion coefficients in 10^{-6} K^{-1}. Thermal properties are computed at 293 K. Data from [39] unless otherwise noted.

		Baskes[1]	Kuo[2]		This Work	
	Expt/	1NN	1NN	2NN		1NN
	DFT	MEAM	MEAM	MEAM	DFT	MEAM
a	4.08				4.05	4.08
E_c^0	3.93				3.60	3.93
B_0	108.3				160.9	108.5
B_0'	5.9 3.81 – 6.29[3]			6.06	5.95	5.32
γ/C_{44}	45.4	41.7	60.9	45.4		45.4
γ'		14.6	23.1			16.1
C_{11}	201.6			201.5		202.0
C_{12}	169.7			169.7		169.7
C_{11}-C_{12}				31.8		32.3
C_{11}-C_{44}				124.3		124.3
G	27[4]					30.0
Y	78[4]					85.2
ν	0.44[4]					0.42
γ_G	2.85[5] 2.91[6]					2.63
v_l						1246
v_t						3379
v_m	2030[7]					1414
T_D	165[4]					163
c_v	25.6[4]					24.6
α_l	14.1[4]					11.6

[1] Reference [38]
[2] Reference [40]
[3] Reference [92]
[4] Reference [93]
[5] Reference [94]
[6] Reference [95] (experimentally assessed values of B_0')

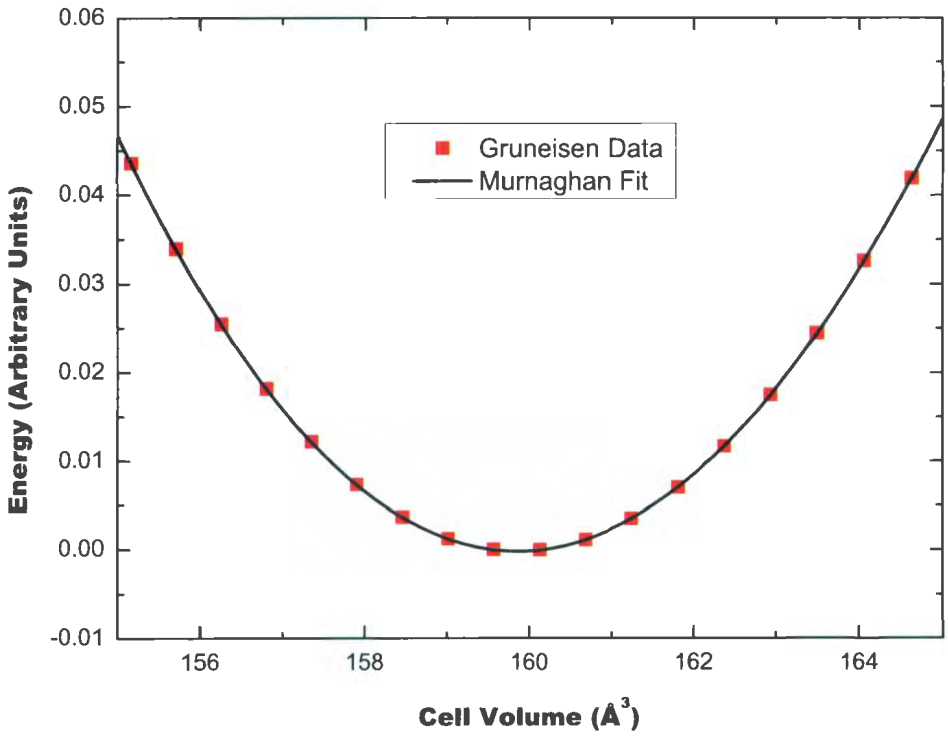

Figure 5.5: Determination of B_0' based on theoretical Grüneisen data.

Continuing the analysis, the structural energy differences are next summarized in Tables 5.7 through 5.9. Again, the results are excellent. For Si, a MAE of 0.03 is observed, compared with the MAE of the first and second nearest neighbour MEAM of 0.09 and 0.02, respectively. Similarly miniscule MAE were observed for Ag and Au. The slightly larger discrepancies observed in the HCP energy difference in Ag and Au are attributed to the fact that the HCP ratio c/a was held in this work at the ideal value of 1.63, but was treated as an optimization parameter by other authors. By optimizing both c and a, a lower total energy may be found.

Table 5.7: Structural energy differences for Si. Cohesive energies are given in eV, lattice constants in Angströms. Data from [37] unless otherwise noted.

STRUCT		EXPT/ DFT	SW	TERS	EDIP	HOEP	1NN MEAM	2NN MEAM	THIS WORK 1NN MEAM
Dia	E	-4.63	-4.63	-4.63	-4.63	-4.63	-4.63	-4.63	-4.63
	a	5.43	5.43	5.43	5.43	5.43	5.43	5.43	5.43
SC	ΔE	0.35	0.29	0.32	0.53	0.29	0.26	0.34	0.37
	a	2.53	2.61	2.54	2.50		2.61	2.62	2.60
BCC	ΔE	0.53	0.30	0.43	1.59	0.72	0.45	0.49	0.55
	a	3.09	3.25	3.08	3.24		3.25	3.14	3.13
FCC	ΔE	0.57	0.42	0.76	1.84	0.70	0.34	0.57	0.68
	a	3.89	4.15	3.90	4.08		4.19	3.98	3.90
HCP	ΔE	0.55	0.32	0.76	0.93	0.67	0.34	0.56	0.68
	a	2.74	3.65	2.76	2.56		2.96	2.82	2.76
	c/a	1.63	0.88	1.63	2.13	2.04	1.64	1.63	1.63

The point defects are next considered and the results are summarized in Tables 5.10, 5.11 and 5.12. The results are exemplary; the best agreement for the majority of the parameters, especially Si interstitials, are observed in this work.

Finally, the surface properties are examined, and are summarized in Tables 5.13 through 5.15. While, in general, the surface energies are consistent with experimental results, this work continues to highlight one of the major failings of the first nearest neighbour MEAM. First observed by Baskes for the Si and Ge systems [36], and later confirmed in general [38], it is evident that the first nearest neighbour MEAM has difficulties describing inward surface relaxations (as represented by the Δd_{12} values). No suitable MEAM parameters could be found in this work which allow for inward relaxations and yet maintain reasonable accuracy for the other fit parameters. The second nearest neighbour MEAM, which exists to correct this flaw,

is clearly better suited for computations of this type. However, there are difficulties associated with the adoption of the second nearest neighbour MEAM, some of which are described in Section 6.2.2.

5.3 Alloys

For the alloy parameterization, the binary cluster properties are first considered, and are summarized in Table 5.16. Binary clusters were chosen due to the availability of experimental data; these were the only properties for the Si:Ag, Si:Au and Ag:Au systems for which experimental data could be found. Given that the Si, Ag and Au elemental parameters were optimized with no consideration for the binary cluster properties, the results are impressive. In general, the bond lengths are highly accurate, while the binding energies are always higher than the experimental result.

Lastly, the structural energy differences are listed in Table 5.17. In general, three unique behaviours are observed. First, in situations where the MEAM underestimates the lattice constant, a, with respect to the DFT result, the cohesive energies and bulk moduli tend to be larger to compensate (eg. B1 structures). In this case, the bulk moduli derivatives are approximately equivalent. Together, these features merely describe a shift in origin of the energy vs. volume curves; this is not entirely unexpected given Figures 5.2a through 5.4a. The second case is the converse of the first: here, the MEAM overestimates the lattice constant, and the cohesive energies and bulk moduli are smaller than their DFT counterparts. In the particular case of the $L1_2$ structures, the bulk moduli derivatives are once again approximately equal, and so the result of these discrepancies is a shift in origin. However, for the

diamond substitutions (cf. Table 4.4), the MEAM bulk moduli derivatives are always larger than those in from DFT. Consequently, the MEAM potential wells for the diamond substitutions are much more steep than those from DFT. Finally, there is the scenario where the lattice constant is approximately equal between the MEAM and DFT computations, as observed in the ternary systems. In this case, the cohesive energies and bulk moduli are roughly equivalent, but the bulk moduli derivatives are larger in the MEAM. To summarize this result, there is no shift in origin, but the MEAM potential well is steeper than that of the DFT. To further quantify the implications of these discrepancies on other physical parameters, additional work is necessary as described in Section 6.2.1.

Table 5.8: Structural energy differences for Ag. Cohesive energies are given in eV, lattice constants in Angströms. Data from [39] unless otherwise noted.

STRUCT		EXPT/ DFT	1NN MEAM*	2NN MEAM	THIS WORK 1NN MEAM
FCC	E	-2.85	-2.85	-2.85	-2.85
	a	4.09	4.09	4.09	4.09
Dia	ΔE		0.46	0.66	0.56
	a		6.37	6.00	6.02
SC	ΔE		0.15	0.31	0.14
	a		2.80	2.67	2.66
BCC	ΔE	0.03 0.04	0.03	0.06	0.04
	a		3.27	3.21	3.21
HCP	ΔE	0.003	0.005	0.005	0.06
	a			2.28	2.91
	c/a			1.64	1.63

Reference [38]

Table 5.9: Structural energy differences for Au. Cohesive energies are given in eV, lattice constants in Angströms. Data from [39] unless otherwise noted.

STRUCT		EXPT/ DFT	BASKES* 1NN MEAM	KUO† 1NN MEAM	2NN MEAM	THIS WORK 1NN MEAM
FCC	E	-3.93	-3.93	-3.93	-3.93	-3.93
	a	4.08	4.08	4.08	4.08	4.08
Dia	ΔE		0.59		0.67	0.74
	a		6.33		5.93	5.98
SC	ΔE		0.12		0.22	0.18
	a		2.79		2.65	2.65
BCC	ΔE	0.04 0.07	0.02	0.02	0.06	0.04
	a		3.27		3.19	3.17
HCP	ΔE	0.003 0.005	0.012	0.021	0.009	0.07
	a				2.28	2.88
	c/a				1.65	1.63

*Reference [36]
†Reference [40]

Table 5.10: Point defect calculations for Si. All entries given in eV. Data from [37] unless otherwise noted.

	EXPT/ DFT	SW	TERS	EDIP	HOEP	1NN MEAM	2NN MEAM	THIS WORK DFT	THIS WORK 1NN MEAM
E_i^f	2.7 – 3.9	2.82	3.70	3.22	3.30	3.19	3.33	3.54	3.66
E_i^{mig}	0.33					0.37			0.35
Q						3.56			4.01
E_f^f (Tet)	3.5 – 4.7	5.25	3.45	4.05	3.11	5.74	4.68		3.48
E_f^f (Hex)	3.2 – 4.4	6.95	4.61	4.16	3.21	7.14	5.78		4.84

*Reference [36]

Table 5.11: Point defect calculations for Ag. All entries given in eV. Data from [39] unless otherwise noted.

			This Work	
	Expt/	2NN		1NN
	DFT	MEAM	DFT	MEAM
E_v^f	1.1	0.94	1.21	1.13
E_v^{mig}	0.67	0.92		0.66
Q	1.77	1.86		1.79
E_I^f (100 DB)		2.86		2.86

Table 5.12: Point defect calculations for Au. All entries given in eV. Data from [39] unless otherwise noted.

			This Work	
	Expt/	2NN		1NN
	DFT	MEAM	DFT	MEAM
E_v^f	0.9	0.90	0.91	0.91
E_v^{mig}	0.8	0.85		0.81
Q	1.7	1.75		1.73
E_I^f (100 DB)		2.93		3.37

Table 5.13: Surface properties as computed for Si. Energies and energy differences are given in eV/Atom, plane spacing ratios in percent. Data from [37] unless otherwise indicated.

	EXPT/ DFT	SW	TERS	1NN MEAM	2NN MEAM	THIS WORK 1NN MEAM
$E(100)$	2.5	2.32	2.13	2.21	2.48	2.13
$E(100)1\times1$	2.47	2.32	2.09	1.81	2.47	1.90
$\Delta E(100)1\times1$	-0.03	0	-0.04	-0.40	-0.01	-0.23
$\Delta d_{1,2}/d$	-5.1	0	7.2		-3.6	10.0
$E(100)2\times1$		0.52	0.61	0.81	0.50	1.01
$\Delta E(100)2\times1$	-2.06 -1.5	-1.80	-1.52	-0.90	-1.98	-1.12
$\Delta d_{1,2}/d$	-24.4	-8.3	-15.6	15.4	-9.0	-1.0
$E(110)$		1.16	1.03	1.69	1.22	1.23
$E(110)1\times1$		1.16	0.99	1.30	1.20	1.10
$\Delta E(110)1\times1$		0	-0.04	-0.39	-0.02	-0.13
$\Delta d_{1,2}/d$		0	-4.3	12.6	-3.5	6.0
$E(110)$	1.56	1.16	1.03		1.23	2.62
$E(111)1\times1$	1.39	1.16	0.96		1.22	1.17
$\Delta E(111)1\times1$	-0.17	0	-0.07		-0.01	-1.45
$\Delta d_{1,2}/d$	-25	0	-20.3		-16.0	-5.0

Table 5.14: Surface properties as computed for Ag. Energies and energy differences are given in eV/Atom (erg/cm^2), plane spacing ratios in percent. $\Delta E(100)$ Hex and $\Delta E(100)1\times2$ take the form **Y** or **N**, where **Y** indicates the reconstruction is energetically favoured, and **N** indicates the converse. Data from [39] unless otherwise indicated.

	EXPT/ DFT	1NN MEAM*	2NN MEAM	THIS WORK 1NN MEAM
E_{poly}	(1320)			
$E(100)$				0.645
$E(100)1\times1$		0.664 (1271)	0.513 (983)	0.618 (1184)
$\Delta E(100)1\times1$				-0.027
$\Delta d_{12}/d$	-2		-2.4	5.1
$E(100)$Hex	**N**		**N**	**N**
$E(110)$				0.802
$E(110)1\times1$		0.911 (1222)	0.753 (1010)	0.778 (1043)
$\Delta E(110)1\times1$				-0.024
$\Delta d_{12}/d$	-7 -11		-10.4	-5.6
$E(110)1\times2$	**N**		**N**	**N**
$E(110)$				4.182
$E(111)1\times1$		1.284 (1087)	0.995 (842)	0.800 (677)
$\Delta E(111)1\times1$				-3.382
$\Delta d_{12}/d$	-2 2		-2.1	1.6

* Reference [38]

Table 5.15: Surface properties as computed for Au. Energies and energy differences are given in eV/Atom (erg/cm^2), plane spacing ratios in percent. $\Delta E(100)$ Hex and $\Delta E(100)$ 1×2 take the form **Y** or **N**, where **Y** indicates the reconstruction is energetically favoured, and **N** indicates the converse. Data from [39] unless otherwise indicated.

	EXPT/ DFT	BASKES* 1NN MEAM	KUO† 1NN MEAM	2NN MEAM	THIS WORK 1NN MEAM
E_{pnik}	(1540)				
$E(100)$					0.594
$E(100)$ 1×1		0.544 (1048)	0.592 (1140)	0.591 (1138)	0.594 (1143)
$\Delta E(100)$ 1×1					0
$\Delta d_{12}/d$	-1			-4.3	-0.1
$E(100)$ Hex	**Y**			**N**	**Y**
$E(110)$					0.779
$E(110)$ 1×1		0.827 (1115)	0.625 (842)	0.875 (1179)	0.733 (988)
$\Delta E(110)$ 1×1					-0.046
$\Delta d_{12}/d$	-9.8			-17.5	-10.2
$E(110)$ 1×2	**Y**			**N**	**N**
$E(110)$					1.841
$E(111)$ 1×1		1.042 (882)	0.437 (372)	1.091 (928)	0.510 (434)
$\Delta E(111)$ 1×1					-1.331
$\Delta d_{12}/d$				-2.7	-3.0

*Reference [38]
†Reference [40]

Table 5.16: Binary cluster properties for various systems. Energies are given in eV/Atom, bond lengths in Angströms.

SYSTEM	PARAM.	EXPT.	DFT	THIS WORK 1NN MEAM
Si_2	E_b	1.66[1]	1.77[1]	2.20
	R^{dist}	2.24[1]	2.28[1]	2.51
Ag_2	E_b	0.825[2]	1.17[2]	1.37
	R^{dist}	2.53[2]	2.52[2]	2.56
Au_2	E_b	1.16[1]	1.155[1]	1.81
	R^{dist}	2.47[1]	2.52[1]	2.42
SiAg	E_b			1.96
	R^{dist}			2.58
SiAu	E_b	1.58[1]	1.71[1]	1.99
	R^{dist}		2.25[1]	2.43
AgAu	E_b	1.04[2]	1.11[2]	1.52
	R^{dist}	2.50[2]	2.54[2]	2.45

[1] Reference [96]
[2] Reference [97]

Table 5.17: Structural energy differences for a variety of compounds. a are given in Angströms, E_f in eV and B_0 in eV/Å^3.

		This Work	
			1NN
System	Parameter	DFT	MEAM
B1	a	5.07	3.18
SiAg	E	3.37	4.52
	B_0	0.564	0.440
	B_0'	5.00	5.10
B1	a	4.94	4.54
SiAu	E	4.27	2.62
	B_0	0.773	0.775
	B_0'	4.47	5.11
B1	a	5.36	4.96
AgAu	E	2.60	3.93
	B_0	0.601	1.071
	B_0'	5.45	5.65
$L1_2$	a	3.98	4.10
Ag_3Si	E	3.38	2.86
	B_0	0.664	0.344
	B_0'	5.26	6.36
$L1_2$	a	3.83	4.45
Si_3Ag	E	4.45	3.16
	B_0	0.552	0.150
	B_0'	5.58	4.37
$L1_2$	a	3.96	4.11
Au_3Si	E	4.14	3.77
	B_0	0.925	0.744
	B_0'	5.04	5.11
$L1_2$	a	3.78	4.12
Si_3Au	E	4.76	3.61
	B_0	0.611	0.631
	B_0'	3.79	5.08
$L1_2$	a	4.03	3.93
Au_3Ag	E	3.51	3.70
	B_0	0.926	0.895
	B_0'	5.80	5.18

System	Parameter	This Work DFT	This Work 1NN MEAM
$L1_2$	a	4.05	4.01
Ag_3Au	E_c	3.48	3.26
	B_0	0.748	0.550
	B_0'	5.55	5.25
Dia. Sub.	a	5.32	5.70
Si_2Ag	E_c	4.17	3.94
	B_0	0.525	0.826
	B_0'	3.93	4.82
Dia. Sub.	a	5.26	5.57
Si_2Au	E_c	4.45	4.35
	B_0	0.570	1.015
	B_0'	3.86	5.44
cI16	a	3.90	4.18
$AuSi_3Ag_3$	E_c	4.05	3.85
	B_0	0.703	0.324
	B_0'	4.90	6.33
$E2_1$	a	4.52	4.53
$AgAuSi_3$	E_c	3.70	3.87
	B_0	0.391	0.363
	B_0'	3.00	7.58
$L2_1$	a	6.29	6.14
$SiAu_2Ag$	E_c	3.77	3.77
	B_0	0.811	0.649
	B_0'	5.80	6.31

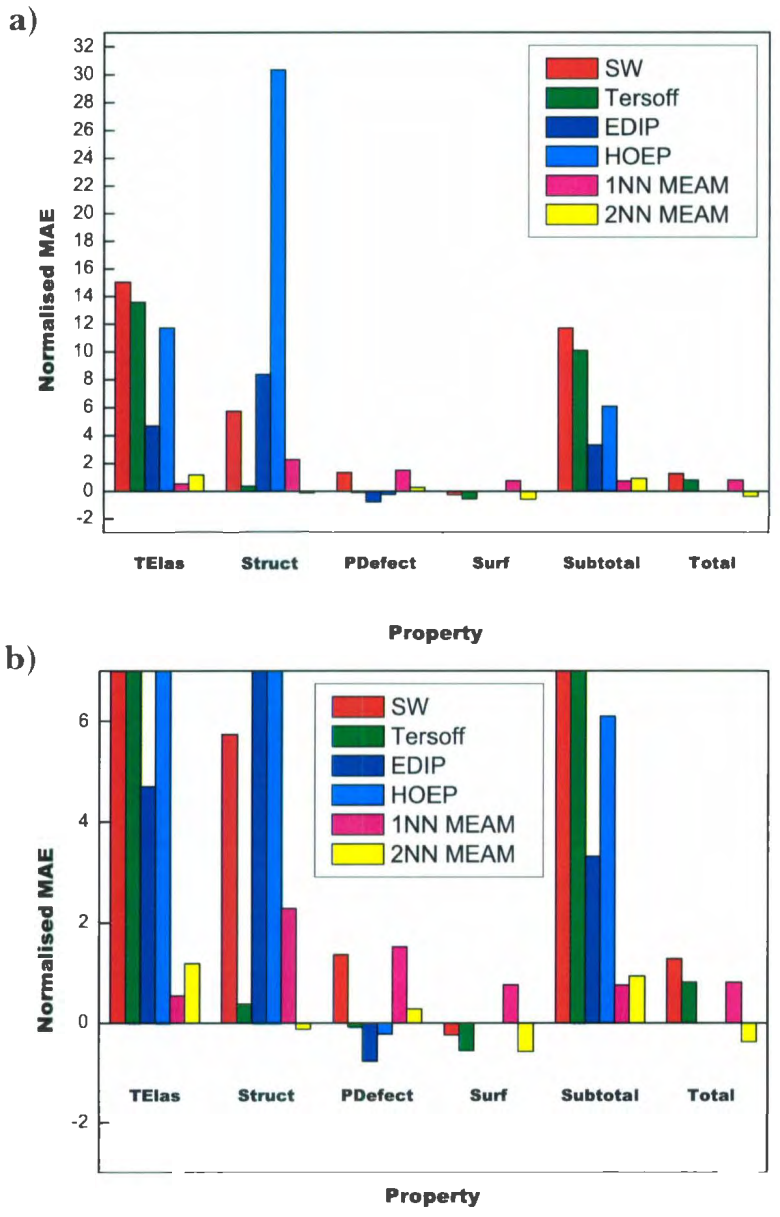

Figure 5.6: Normalised ($MAE_{\prime\prime}$ $MAE_{\text{this work}}$) MAEs for silicon thermoelastic (TElas), structural (Struct), point defect (PDefect) and surface (Surf) properties. Subtotal represents the MAEs of all properties *except* surface properties; Total represents the MAEs of all properties. $y = 0$ represents this work: bars below the y-axis represent better fits than this work, bars above the y-axis represent an improvement in this work. a) shows the data to scale. b) shows a truncated data set to highlight the minimal improvements observed in other work.

6. Conclusions

6.1 Summary

In this work, first nearest neighbour MEAM parameters for Si, Ag, Au, SiAg, SiAu and SiAgAu systems have been provided. These parameter sets have been fit according to a variety of thermoelastic, structural, point defect, surface and cluster properties. In each case, the set of parameters for Si, Ag, Au and SiAu demonstrate an improvement over existing parameterizations. Finally, new parameterizations for SiAg and SiAgAu systems are presented.

6.2 Future Work

6.2.1 DFT Pseudopotential Refinement

Perhaps the most obvious area for improvement in this work involve the DFT pseudopotentials. As shown in Figures 5.2a, 5.3a and 5.4a, the current pseudopotentials all shift the origin of the energy vs. volume graphs. That is, the equilibrium cohesive energy and lattice constants obtained from the DFT calculations are not in exact agreement with experimental values. Given that these elemental pseudopotentials are used to describe the properties of binary and ternary alloys, these discrepancies

are further compounded. It may also be prudent to compute several other physical parameters using DFT. Features such as the elastic constants, surface properties and point defects are readily calculated, but are especially costly due to the large supercells required for such a computation. One may surmise that improved DFT pseudopotentials will allow for more accurate alloy properties, and thus the MEAM fits may be enhanced.

6.2.2 Second Nearest Neighbour MEAM

As described in Section 5.2, the first nearest neighbour MEAM is unable to properly describe free surface relaxations. As one of the main goals of this work is to study the structure, morphology and composition of silicon-based systems with an atomically flat gold surface layer, it may be necessary to use a second nearest neighbour approach. There are, however, several obstacles to overcome should this be the case. Aside from the fact that the second nearest neighbour MEAM is computationally more costly, the present MEAM model is unable to treat composite systems within the second nearest neighbour formalism. To that end, equations describing the B1 structure must first be derived for the second nearest neighbour MEAM (cf. Equations 3.13 and 3.26), and these equations must then be implemented and tested in a software such as LAMMPS.

6.2.3 Interfacial Stress Analysis

The primary goal of this work is to determine an empirical relationship for interfacial stress between the substrate silicon layer and the gold/silver tie layers which is

dependent upon the tie layer thickness, deposition rate, temperature and annealing time. From our experimental work, we have established that the process of depositing the tie layer(s) onto the silicon substrate results in an interfacial stress which in turn leads to a net curvature of the cantilever. It has been qualitatively observed that the stress may be tensile or compressive, and resultantly the cantilever may bend upwards or downwards. Thus far, experiments have been unable to quantify, or predict, the exact nature of the interfacial stress. In this work, a series of simulations are proposed which will determine this relationship. To begin, the most basic system will be studied, consisting of a long, thin silicon substrate proportional to a cantilever, and a single gold tie layer at a temperature of 293K, as shown schematically in Figure 6.1. This system will be periodic along x, and non-periodic along y and z. By varying the thickness of the gold tie layer by introducing gold atoms at an appropriate time interval and kinetic energy (corresponding to deposition rate and temperature, respectively), one should be able to map the stress response of the system as a function of tie layer thickness. Next, the system temperature will be modified, and the preceding experiment repeated. The system will be initially set at 293K, and a multitude of temperature increases over differing timescales tested for a variety of thicknesses (both by increasing the kinetic energy of the introduced atoms to simulate increases due to deposition, and by increasing the system temperature to simulate annealing). In this way, the model will now account for interfacial stress as a function of both film thickness and deposition temperature/annealing time. Finally, the above simulations will be repeated for tie layers of silver, and silver-gold composites. The final empirical relationships will be used to predict deposition parameters which will yield microcantilevers with no net curvature. These will then be fabricated in the lab to confirm the model.

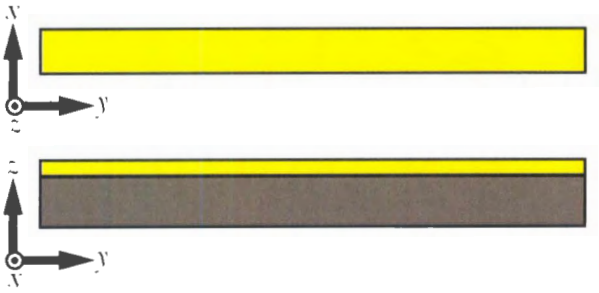

Figure 6.1: Schematic representation of the system used in the simulations described in Section 6.2.3. In this figure, the grey area depicts the silicon substrate, and the yellow area the gold tie layer.

6.2.4 Surface Analysis

In tandem with the simulations detailed in Section 6.2.3, the second crucial focus of this work is to predict the composition of the tie layer(s) which, in addition to inducing no net curvature, allows for an atomically flat gold surface layer. The surface features of the tie layer are critical as they determine the characteristic properties, such as the self-assembly stacking, of the organic detection layer(s). To begin, configurations which mimic those produced in our lab will be studied. The initial system should approximate a 1 μm thick silicon substrate, and a 20 nm thick gold tie layer, which are the approximate dimensions of the sensors presently fabricated in our lab. It is suggested that for these simulations, the silicon substrate be terminated at a thickness of 20 nm and the bottom layers frozen to simulate bulk. While this will prevent curvature studies (which is why Sections 6.2.3 and 6.2.4 must be completed concurrently), it will allow for a larger surface area to be studied. With a 50 nm by 50 nm surface, the resultant system would be comprised of roughly five to six million atoms; a system of this size can be simulated in approximately two

weeks with our present facilities[1]. Simulations should be run by applying various temperature gradients, as in Section 6.2.3, to appropriately mimic annealing conditions. The resultant surface positions may then be used to construct pseudo-STM images, which should be comparable to STM data collected in our lab. Specifically, the simulations should recreate the outstanding surface features, such as dominant structure, clustering, islands and terraces, etc. Should this be the case, predictive simulations may be executed to ascertain the tie layer(s) composition(s) which provides the flattest possible surface for the organic receptive layer. In conjunction with the simulations in Section 6.2.3, the final result should yield an atomically flat surface layer with no net curvature: the ideal sensing platform.

6.2.5 Oscillating Cantilever Analysis

Recent work [98] has shown the surface structure of the tie layer to be a function of position along the length of the cantilever. That is, the surface structure at the stable cantilever chip surface differs from that of the cantilever tip, and at all points in between. Until this discovery, it had been assumed that the surface structure was identical at all points along the lever. The authors hypothesized that these discrepancies may be attributed to minute thermal oscillations of the cantilever during deposition, which would change both the incident angle of depositing atoms as well as their kinetic energies. As an extension to the simulations performed in Section 6.2.3, a trivial modification may be made to account for an oscillating substrate.

[1]Estimation based on the execution times to converge similarly sized systems deployed on ACENet clusters across 16 to 32 cores.

In so doing, these results may assist to confirm the authors' original reasoning, or imply an alternate mechanism for the discrepancies in surface structures altogether.

6.2.6 MEAM Sulfur Potential

Once the substrate/tie layer system has been sufficiently described, it remains to study the entire cantilever platform. For this purpose, a MEAM potential for Sulfur will necessarily be added to the present Si/Ag/Au potentials to describe the organic thiol adsorption to the tie layer surface. Once determined, a hybrid approach, similar to ONIOM (***o***ur own ***n***-layered ***i***ntegrated molecular ***o***rbital and ***m***olecular mechanics) [99] must be adopted. The ONIOM method treats a complicated system as a discrete set of constituent components: an active part consisting of the critical atoms to be studied, a semi-active part consisting of those atoms which most contribute to the electronic and structural properties of the critical atoms and a non-active part consisting of the remainder of the atoms in the system. In this way, the active atoms may be treated with the highest level of theory at the highest computational cost, the semi-active atoms with the next highest level of theory and so forth.

In this work, a hybrid approach using the MEAM and a suitable organic potential (CHARMM, Amber, ECEPP, etc.) is proposed. The MEAM potentials will be used to describe the Silicon substrate, tie layers and adsorbed Sulfur atoms, while the organic potential will be used to describe the remainder of the organic receptive chains. It is expected that the organic potentials will provide the proper attractive (or repulsive) forces between receptor chains in order to strain the adsorbed Sulfur atoms. In turn, the MEAM will optimize the position of the Sulfur and Gold surface

atoms to minimize the energy of the system. If successful, this hybrid method will allow the entire cantilever platform to be simulated. One may then proceed to optimize the substrate/tie layer/receptor layer system until a system with no net curvature is obtained. This would provide a complete cantilever sensor which would require no calibration before use, and would be a momentous step towards the commercial adoption of the cantilever sensor platform.

BIBLIOGRAPHY

1. Battiston, F.M., J.P. Ramseyera, H.P. Langa, M.K. Ballera, C. Gerberb, J.K. Gimzewskib, E. Meyera and H.J. Güntherodt, Sens. Actuators B, 2001. B76(1-3): 393-402.

2. Ji, H.F. and T. Thundat, Biosens. Bioelectron., 2002. 17(4): 337-343.

3. Wachter, E.A. and T. Thundat, Rev. Sci. Instrum., 1995. 66(6): 3662-3667.

4. Yang, Y., H.F. Ji, and T. Thundat, J. Am. Chem. Soc., 2003. 125: 1124-1125.

5. Bottomley, L.A., M. Ghosh, S. Shen, R. Saul, S. Kossek, and G.W. Pace, 2002, Protiveris Inc.

6. Grogan, C., R. Raiteri, G.M. O'Connor, T.J. Glynn, V. Cunningham, M. Kane, M. Charlton and D. Leech, Biosens. Bioelectron., 2002. 17(3): 201-207.

7. Hwang, K.S., K. Eom, J.H. Lee, D.W. Chun, B.H. Cha, D.S. Yoon, T.S. Kim and J.H. Park, Korea Institute of Science and Technology: Seoul. 15.

8. Su, M., S. Li, and V.P. Dravid, Applied Physics Letters, 2003. 82(20): 3562-3564.

9. Subramanian, A., P.I. Oden, S.J. Kennel, K.B. Jacobson, R.J. Warmack, T. Thundat, and M.J. Doktycz, Applied Physics Letters, 2002. 81(2): 385-387.

10. Thundat, T., Scanning, 2001. 23(2): 129.

11. Dareinga, D.W. and T. Thundat, Journal of Applied Physics, 2005. 97.

12. Godin, M., V. Tabard-Cossa, P. Grütter and P. Williams, Applied Physics Letters, 2001. 79(4): 551-553.

13. Hu, Z., T. Thundat, and R.J. Warmack, Journal of Applied Physics, 2001. 90(1): 427-431.

14. Finot, E., T. Thundat, E. Lesniewska and J.P. Goudonnet, Ultramicroscopy, 2001. 86(1-2): 175-180.

15. Ji, H.F., K.M. Hansen, Z. Hu and T. Thundat, Sensors and Actuators B, 2001. B72(3): 233-238.

16. Bendavid, A., P.J. Martin and L. Wieczorek, Thin Solid Films, 1999. 354: 169-175

17. Nuzzo, R.G., F.A. Fusco and D.L. Allara, J. Am. Chem. Soc., 1987. 109: 2358

18. Godin, M., P.J. Williams, V. Tabard-Cossa, O. Laroche, L.Y. Beaulieu, R.B. Lennox and P. Grütter, Langmuir, 2004. 20: 7090-7096.

19. Spaepen, F., Acta Mater, 2000. 18: 31-42.

20. The MEMS handbook, ed. M. Gad-el-Hak. 2002: CRC Press.

21. Ohring, M., Materials science of thin films. Second ed. 2002: Academic Press.

22. Hsueh, C.H., Journal of Applied Physics, 2002. 91(12): 9652-9656.

23. Huang, S. and X. Zhang, Sensors and Actuators A, 2006.

24. Min, Y.H. and Y.K. Kim, Journal of Micromechanics and Microengineering, 2000. 10: 314–321.

25. Moulard, G., G. Contoux, G. Gardet, G. Motyl and M. Courbon, Surface and Coatings Technology, 1997. 97: 206-211.

26. Moulard, G., G. Contoux, G. Motyl, G. Gardet and M. Courbon, J. Vac. Sci. Technol., 1998. 16(2): 736-742.

27. Sader, J.E., Journal of Applied Physics, 2001. 89(5): 2911-2921.

28. Senez, V., T. Hoffmann, A. Armigliato and I. DeWolf, Smart Materials and Structures, 2006. 15: S47–S56.

29. Son, D., J.H. Jeong, and D. Kwon, Thin Solid Films, 2003. 437: 182-187.

30. Zhang, Y., Q. Ren, and Y.F. Zhao, Journal of Physics D: Applied Physics, 2004. 37: 2140-2145.

31. Zhang, Y. and Y.P. Zhao, Microsyst. Technol., 2005. 12: 357–364.

32. Huang, S., B. Li, and X. Zhang, Sensors and Actuators A, 2006. 130-131: 331-339.

33. Kang, T.J., J.G. Kim, J.S. Lee, J.H. Lee, J.H. Hahn, H.Y. Lee and Y.H. Kim, Journal of Micromechanics and Microengineering, 2005. 15: 2469–2478.

34. Koster, M. and H.M. Urbassek, Phys. Rev. B, 2000. 62(16).

35. Starman, L.A., Air Force Institute of Technology: Ohio. 2002.

36. Baskes, M.I., J.S. Nelson and A.F. Wright, Phys. Rev. B, 1989. 40: 6085.

37. Lee, B.J., Comp. Coup. Phase. Diag. and Thermochem., 2007. 31: 95–104.

38. Baskes, M.I., Phys. Rev. B, 1992. 46(5): 2727–2742.

39. Lee, B.J., J.H. Shim and M.I. Baskes, Phys. Rev. B, 2003. 68: 144112.

40. Kuo, C.L. and P. Clancy, Surf. Sci., 2004. 551: 39–58.

41. Oura, K. and T. Hanawa, Surf. Sci., 1979. 82: 202.

42. Hanbucken, M., Z. Imam, J.J. Metois and G. Le Lay, Surf. Sci., 1985. 162: 628.

43. Narusawa, T., K. Kinoshita, W.M. Gibson and A. Hiraki, J. Vac. Sci. Tech., 1981. 18: 872.

44. Yang, G., J.H. Kim, S. Yang and A.H. Weiss, Surf. Sci., 1996. 367: 15.

45. Kim, J.H., G. Yang, S. Yang and A.H. Weiss, Surf. Sci., 2001. 475: 37.

46. Taleb-Ibrahimi, A., C.A. Sebenne, D. Bolmont and P. Chen, Surf. Sci, 1984. 146: 229.

47. Molodtsov, S.L., C. Laubschat and G. Kaindl, Phys. Rev. B, 1991. 44: 8850.

48. Yeh, J.J., J. Hwang, K. Bertness, D.J. Friedman, R. Cao and I. Lindau, Phys. Rev. Lett., 1993. 70: 3768.

49. Brillson, L.J., A.D. Katnani, M. Kelly and G. Margaritondo, J. Vac. Sci. Tech. A, 1984. 2: 551.

50. Payne, M.C., M.P. Teter, D.C. Allan, T.A. Arias and J.D. Joannopoulos. Rev. Mod. Phys., 1992. 64: 4.

51. Born, M. and V. A. Fock, Zeitschrift für Physik a Hadrons and Nuclei, 1928. 51(3–4): 165–180.

52. Born, M., and J.R. Oppenheimer. Ann. Physik, 1927. 84: 457.

53. Hohenberg, P. and W. Kohn, Phys. Rev., 1964. 136: 864B.

54. Kohn, W. and L.J. Sham, Phys. Rev., 1965. 140: 1133A.

55. Perdew, J.P., K. Burke, M. Ernzerhof. Phys. Rev. Let., 1996. 77: 18.

56. Perdew, J.P., J.A. Chevary, S.H. Vosko, K.A. Jackson, M.R. Pederson, D.J. Singh and C. Fiolhais, Phys. Rev. B, 1993. 46: 6671; 48: 4878E.

57. Becke, A.D., J. Chem. Phys., 1992. 96: 2155.

58. Proynov, E.I., E. Ruiz, A. Vela and D.R. Salahub, Int. J. Quant. Chem., 1995. S29: 61.

59. Hammer, B., K.W. Jacobsen and J.K. Norskov, Phys. Rev. Let., 1993. 70: 3971.

60. Hamann, D.R., Phys. Rev. Let., 1996. 76: 660.

61. Ozolins, V. and M. Korling, Phys. Rev. B, 1993. 48: 18304.

62. Filippi, C., D.J. Singh, and C. Umrigar, Phys. Rev. B, 1994. 50: 14947.

63. Chadi, D.J. and M.L. Cohen, Phys. Rev. B, 1973. 8: 5747.

64. Joannopolous, J.D. and M.L. Cohen, J. Phys. C, 1973. 12: 4409.

65. Monkhorst, H.J. and J.D. Pack, Phys. Rev. B, 1976. 13: 5188.

66. Evarestov, R.A. and V.P. Smirnov, Phys. Stat. Solidi, 1983. 119: 9.

67. Robertson, I.J. and M.C. Payne, J.Phys. Cond. Mat., 1990. 2: 9837; 1991. 3: 8841.

68. Francis, G.P. and M.C. Payne, J. Phys. Cond. Mat., 1990. 17: 1643.

69. Rappe, A.M., K.M. Rabe, E. Kaxiras and J.D. Joannopoulos, Phys. Rev. B, 1990. 41: 1227.

70. Trouillier, N. and J.L. Martins, Phys. Rev. B, 1991. 43: 1993.

71. Vanderbilt, D., Phys. Rev. B, 1990. 41: 7892.

72. Stott, M.J. and E. Zaremba, Phys. Rev. B, 1980. 22: 1564.

73. Daw, M.S. and M.I. Baskes, Phys. Rev. Let., 1983. 50: 17.

74. Daw, M.S. and M.I. Baskes, Phys. Rev. B, 1984. 29: 12.

75. Baskes, M.I., Phys. Rev. Let., 1987. 59: 2666.

76. Banerjea, A. and J.R. Smith, Phys. Rev. B, 1988. 37: 6632.

77. Rose, J.H., J.R. Smith, F. Guinea and J. Ferrante, Phys. Rev. B, 1984. 29: 2963.

78. Shin, Y., M. Scheffler and B.D. Yu, (M)EAM Workshop At Eindhoven, 2002.

79. Murnaghan, F.D., Proceedings of the Natl. Acad. Sci., 1944. 30: 244.

80. Tyuterev, V.G. and N. Vast, Elsevier Sci., 2005.

81. Birch, F., Phys. Rev., 1947. 71: 809.

82. Ashcroft, N.W. and N.D. Mermin, Solid State Physics, Thomson Learning, 1976.

83. Mayer, B., H. Anton, E. Bott, M. Methfessel, J. Sticht, J. Harris and P.C. Schmidt, Intermetallics, 2003. 11: 23.

84. Eliezer, S., A. Ghatak and H. Hora, Fundamentals of Equations of State, World Scientific, 2002.

85. Sato, K., T. Yoshiie, Y. Satoh, Q. Xu and M. Kiritani, Mat. Sci. Eng., 2003. A350: 220.

86. Breuer, S.J. and P.R. Briddon, Phys. Rev. B, 1995. 51: 11.

87. Was, G.S., Fundamentals of Radiation Materials Science: Metals and Alloys, Springer, 2007.

88. Gonze, X., J.M. Beuken, R. Caracas, F. Detraux, M. Fuchs, G.M. Rignanese, L. Sindic, M. Verstraete, G. Zerah, F. Jollet, M. Torrent, A. Roy, M. Mikami, P. Ghosez, J.Y. Raty and D.C. Allan, Comp. Mat. Sci., 2002. 25: 478. (http://www.abinit.org)

89. Gonze, X., G.M. Rignanese, M. Verstraete, J.M. Beuken, Y. Pouillon, R. Caracas, F. Jollet, M. Torrent, G. Zerah, M. Mikami, P. Ghosez, M. Veithen, J.Y. Raty, V. Olevano, F. Bruneval, L. Reining, R. Godby, G. Onida, D.R. Hamann and D.C. Allan, Zeit. Krist., 2005. 220: 558.

90. OPIUM Pseudopotential Generation Project. (http://opium.sourceforge.net)

91. Plimpton, S.J., J. Comp. Phys., 1995. 117: 1 (http://lammps.sandia.gov)

92. Landolt-Bornstein Substance/Property Index (http://lb.chemie.uni-hamburg.de)

93. Brugger, K. and T.C. Fritz, Phys. Rev., 1967. 157(3): 524-531.

94. Wallace, D.C., Thermodynamics of Crystals. Wiley, 1972.

95. Raju, S., E. Mohandas and V. S. Raghunathan, J. Phys. Chem. Sol., 1997. 58(9): 1367-1373.

96. Majumder, C., Phys. Rev. B, 2007. 75: 235409.

97. Zhao, G.F. and Z. Zeng, J. Chem. Phys., 2006. 125: 014303.

98. Lacey, J., R. Stevens, and L.Y. Beaulieu, J. Appl. Phys., 2009. 105: 014508.

99. Svensson,M., S. Humbel, R.D.J. Froese, T. Mastubara, S. Sieber, and K. Morokuma, J. Phys. Chem., 1996. 100: 19357.